The Astrophysical Journal, 755:177 (19pp), 2012 August 20 doi:10.1088/0004-637X/755/2/177

A MULTI-WAVELENGTH HIGH-RESOLUTION STUDY OF THE S255 STAR-FORMING REGION: GENERAL STRUCTURE AND KINEMATICS

I. Zinchenko[1,2], S.-Y. Liu[3], Y.-N. Su[3], S. Kurtz[4], D. K. Ojha[5], M. R. Samal[6], and S. K. Ghosh[7]
[1] Institute of Applied Physics of the Russian Academy of Sciences, 46 Ulyanov St., Nizhny Novgorod 603950, Russia; zin@appl.sci-nnov.ru
[2] Faculty of Radio Physics, Department of Radio Wave Propagation and Radio Astronomy, Nizhny Novgorod University, 23 Gagarin Av., Nizhny Novgorod 603950, Russia
[3] Institute of Astronomy and Astrophysics, Academia Sinica. P.O. Box 23-141, Taipei 10617, Taiwan, Republic of China
[4] Centro de Radioastronomía y Astrofísica, Universidad Nacional Autónoma de México, Morelia, Michoacán, Mexico
[5] Infrared Astronomy Group, Department of Astronomy and Astrophysics, Tata Institute of Fundamental Research, Homi Bhabha Road, Colaba, Mumbai (Bombay)-400005, India
[6] Laboratoire d'Astrophysique de Marseille (UMR 6110 CNRS & Université de Provence), 38 Rue F. Joliot-Curie, 13388 Marseille Cedex 13, France
[7] National Centre for Radio Astrophysics, Tata Institute of Fundamental Research, Pune 411007, India
Received 2012 March 30; accepted 2012 June 22; published 2012 August 7

ABSTRACT

We present observational data for two main components (S255IR and S255N) of the S255 high mass star-forming region in continuum and molecular lines obtained at 1.3 mm and 1.1 mm with the Submillimeter Array (SMA), at 1.3 cm with the Very Large Array, and at 23 and 50 cm with the Giant Metrewave Radio Telescope. The angular resolution was from ∼2″ to ∼5″ for all instruments. With the SMA we detected a total of about 50 spectral lines of 20 different molecules (including isotopologues). About half of the lines and half of the species (in particular N_2H^+, SiO, $C^{34}S$, DCN, DNC, DCO^+, HC_3N, H_2CO, H_2CS, SO_2) have not been previously reported in S255IR and partly in S255N at high angular resolution. Our data reveal several new clumps in the S255IR and S255N areas through their millimeter wave continuum emission. Masses of these clumps are estimated at a few solar masses. The line widths greatly exceed expected thermal widths. These clumps have practically no association with NIR or radio continuum sources, implying a very early stage of evolution. At the same time, our SiO data indicate the presence of high-velocity outflows related to some of these clumps. In some cases, strong molecular emission at velocities of the quiescent gas has no detectable counterpart in the continuum. We discuss the main features of the distribution of NH_3, N_2H^+, and deuterated molecules. We estimate properties of decimeter wave radio continuum sources and their relationship with the molecular material.

Key words: astrochemistry – H II regions – instrumentation: interferometers – ISM: clouds – ISM: molecules – stars: formation

Online-only material: color figures

1. INTRODUCTION

Despite their great importance in almost all areas of astronomy, the formation of stars larger than 8–10 $M_\odot$ is still poorly understood. In part this is because high-mass star formation (HMSF) regions are more distant, more active, and shorter lived than their low-mass counterparts. Nevertheless, enhanced attention has been paid recently to the earliest phases of massive star formation. So far, few young HMSF cores have been studied in detail and it is important to extend the list of such objects, especially considering the large variety of processes that probably lead to the formation of a massive star.

S255 is an H II region associated with a dense core at a commonly accepted distance of 2.5 kpc (Russeil et al. 2007; Ojha et al. 2011), which we adopt here, too. We note, however, that Rygl et al. (2010) report a distance of 1.6 kpc based on trigonometric parallax measurements of methanol masers. The core consists of two main components (S255IR and S255N) separated by slightly over 1′. Our team has previously acquired molecular line observations using single-dish instruments (OSO-20 m, IRAM-30 m, NRAO-12 m). With angular resolution from about 1′ to 10″ (Zinchenko et al. 2009), we obtained $M \sim 300\ M_\odot$, $n \sim 2\times10^5$ cm^{-3}, $T_{\rm kin} \sim 40$ K, and $\Delta V \sim 2$ km s^{-1} for both components. While both components show evidence for cool, massive clumps, their evolutionary states appear to be quite different. S255IR is bright (>70 Jy) in all the *Midcourse Space Experiment* (*MSX*) bands and contains a near-IR cluster of early-B-type stars (Howard et al. 1997; Itoh et al. 2001), a cluster of compact H II regions (Snell & Bally 1986), and a wealth of complex H_2 emission features (Miralles et al. 1997). In contrast, S255N (also called Sh2-255 FIR1 and G192.60-MM1) contains a single cometary UC H II region (e.g., Kurtz et al. 1994), and is undetected by *MSX* at wavelengths shorter than 21 μm (Crowther & Conti 2003). Very Large Array (VLA) and Submillimeter Array (SMA) observations in the continuum, several molecular lines, and water maser emission (Cyganowski et al. 2007) indicate the presence of a massive protocluster in this region. The chemical compositions of S255IR and S255N also appear significantly different (Lintott et al. 2005; Zinchenko et al. 2009). While the CS and HCN abundances are very similar, the abundances of NH_3, N_2H^+, HCO^+, and some other molecules in these components differ significantly.

Recently, both components were studied with the SMA at 1.3 mm in CO, ^{13}CO, $C^{18}O$, CH_3OH, CH_3CN, and some other lines (Wang et al. 2011). These observations revealed three continuum clumps in the S255IR area and high-velocity collimated outflows in both regions. The star population in this complex was studied most recently by Ojha et al. (2011) on the basis of optical and NIR observations. They found a number of new young stellar object (YSO) candidates with a large spread in ages, indicating a scenario of induced star formation.

In general, this star-forming complex represents an excellent laboratory for studies of different stages of massive star formation. Our goal is to investigate further the structure, physical properties, and chemistry of this area on small scales by observations of important molecular tracers like NH_3 (which is a convenient "thermometer" for dense molecular cores and provides information on their density and kinematics, too—e.g., Ho & Townes 1983; Walmsley & Ungerechts 1983), N_2H^+, SiO, deuterated molecules, etc. In addition we want to investigate in more detail the distribution and properties of ionized gas in this region in order to trace the interaction of massive YSOs and outflows with the surrounding medium.

In this paper, we present observational data obtained at 1.3 mm and 1.1 mm with the SMA in the compact configuration (both in various lines and in continuum), with the VLA at 1.3 cm (in ammonia lines) and with the Giant Metrewave Radio Telescope (GMRT) at 23 and 50 cm in continuum. We also discuss the general structure and kinematics of the complex and derive basic physical parameters of the observed features.

2. OBSERVATIONS AND DATA REDUCTION

2.1. SMA

The S255 complex, including S255N and S255IR, was observed with the SMA in its compact configuration on 2010 April 7 and April 14 at 224.8 GHz and 283.9 GHz, respectively. Two fields, one centered at S255N ($06^h12^m53^s.669$, $18^\circ00'26''.903$) and one centered at S255IR ($06^h12^m53^s.800$, $17^\circ59'22''.097$) were interleaved throughout the observations. The primary HPBW of the SMA antennas is $55''$–$45''$ at these frequencies. Typical system temperatures on source were between 90 K and 160 K for the 224.8 GHz track, and between 100 K and 200 K for the 283.9 GHz track. The resulting uv-coverage ranges from 6 kλ to 50 kλ and 8 kλ to 65 kλ for the 224.8 GHz and 283.9 GHz tracks, respectively. 3C273 was used as the bandpass calibrator for both tracks, and 0530+135 as well as 0750+125 were used as the complex phase and amplitude gain calibrator. The gain calibrator flux scale, calibrated against Mars, was found to be consistent within 5% with the SMA calibrator database and estimated to be accurate within 20%. In the 224.8 GHz observation, a total of 8 GHz (216.8–220.8 GHz in the lower sideband (LSB) and 228.8–232.8 GHz in the upper sideband (USB)) was observed with the SMA bandwidth doubling correlator configuration. A number of different spectral resolutions, with a maximum resolution of 0.53 km s^{-1}, were employed for different molecular lines. The 283.9 GHz observation covered 277.9–279.9 GHz in the LSB and 287.9–289.9 GHz in the USB. The data calibration was carried out with the IDL superset MIR (Scoville et al. 1993), and subsequent imaging and analysis were done in MIRIAD (Sault et al. 1995). With robust weighting for the continuum and line data, the synthesized beam sizes are approximately $3''.8 \times 3''.0$ (P.A. 60°) at 1.3 mm and $2''.9 \times 2''.6$ (P.A. 40°) at 1.1 mm. The noise level is ∼8 mJy $beam^{-1}$ in the 1.1 mm continuum image and roughly 60 mJy $beam^{-1}$ and 100 mJy $beam^{-1}$ in the line cubes at 2.0 km s^{-1} spectral resolution at 220–230 GHz and 280–290 GHz, respectively.

2.2. VLA

The VLA observations (program AZ186) were made on 2009 November 13 (S255N) and 21 (S255IR) with the array in the D-configuration. The pointing centers for S255N and S255IR in J2000 coordinates were $06^h12^m53^s.7$ $+18^\circ00'27''$ and $06^h12^m54^s.0$ $+17^\circ59'22''$, respectively. At the observing frequency the VLA primary beam is approximately 2 arcmin. The correlator was in the 1IF mode, measuring right circular polarization with a 6.25 MHz bandwidth and 127 channels of 48.8 kHz each. The ammonia (1,1) and (2,2) lines were observed, with rest frequencies of 23,693.7955 and 23,721.9336 MHz. 3C147 was observed as the flux calibrator, and J0530+135 was observed as the phase and bandpass calibrator. The assumed flux density for 3C147 was 1.700 Jy and the bootstrapped flux density for J0530+135 was 1.439 ± 0.015 Jy. The angular resolution of the image cubes was $2''.61 \times 2''.51$ (P.A. $-65^\circ.6$). The approximate rms noise of the cube was 3.5 mJy $beam^{-1}$. The on-source time was approximately one-half hour in each transition.

2.3. GMRT

The radio continuum interferometric observations at 610 MHz and 1280 MHz were carried out on 2009 May 8 and 2009 September 8, using the GMRT array. The GMRT has a "Y"-shaped hybrid configuration of 30 antennas, each 45 m in diameter. There are six antennas along each of the three arms (with arm length of ∼14 km). The remaining 12 antennas are located in a random and compact (∼1 km × 1 km) arrangement near the center. Details of the GMRT antennas and their configurations can be found in Swarup et al. (1991). The largest angular scales to which the GMRT is sensitive are $8'$ and $17'$ at 1280 and 610 MHz, respectively.

Flux and phase calibrators were observed to derive the phase and amplitude gains of the antennas. 3C147 was used as the flux calibrator, while the phase calibrators were 0503+020 and 0632+103 at 610 MHz and 1280 MHz, respectively. The data analysis was done using AIPS. Corrupted data were identified and flagged. The estimated uncertainty of the flux calibration is within 7% at both frequencies. Images of the field were formed by the Fourier inversion and cleaning algorithm task IMAGR. Several iterations of self-calibration were carried out to remove the residual effects of atmospheric and ionospheric phase corruption and to improve the quality of the maps. The high-resolution images ($6''.4 \times 4''.8$ at 610 MHz and $5''.2 \times 3''.8$ at 1280 MHz) were made with a Briggs weighting function halfway between uniform and natural weighting (robust factor = −0.5 to 0), which is a good compromise between angular resolution and sensitivity.

3. RESULTS

With the SMA we detected about 50 spectral lines of 20 different molecules (including isotopologues). About half of the lines and half of the species (in particular ^{12}CO, ^{13}CO, $C^{18}O$, CH_3OH, CH_3CN, ^{13}CS, HNCO, SO, OCS) were previously observed in this area with the SMA by Wang et al. (2011). We do not discuss these lines in detail; rather, we compare their results with our line detections. Our additional to Wang et al. (2011) observations include lines of N_2H^+, SiO, $C^{34}S$, DCN, DNC, DCO^+, HC_3N, H_2CO, H_2CS, SO_2 as well as additional transitions of CH_3OH, HNCO, and OCS. A list of these lines, including their frequencies and lower energy levels, is given in Table 1. Some of them (marked in Table 1) were observed earlier in S255N at the SMA by Cyganowski et al. (2007). Nevertheless, they have not been observed in S255IR and our data show many new features in these lines in S255N, which are presented and discussed below. In addition, we observed the (1,1) and (2,2) ammonia lines with the VLA. Here, we

Table 1
List of Molecular Transitions Observed at the SMA in either S255IR or S255N in Addition to Those Observed by Wang et al. (2011)

Molecule	Transition	Frequency (GHz)	E_l (cm^{-1})
CH_3OH	5_1–4_2 E	216.945521	31.596
	6_1–7_2 A^-	217.299205	252.644
	4_2–3_1E	218.440050	24.310[a]
	10_2–9_3 A^+	232.418571	107.208
	9_{-1}–8_0 E	278.304575	67.150
	14_4–15_3 E	278.599037	226.775
	11_2–10_3 A^-	279.351887	123.338
	6_0–5_0E	289.939386	33.316
SiO	5–4	217.104984	14.484[a]
$C^{34}S$	6–5	289.209068	24.119
DCN	3–2	217.238530	7.246[a]
	4–3	289.644907	14.493
DNC	3–2	228.910471	7.636
DCO^+	4–3	288.143858	14.418
HNCO	$10_{1,10}$–$9_{1,9}$	218.981170	62.949
HC_3N	24–23	218.324711	83.755[a]
H_2CS	$8_{1,7}$–$7_{1,6}$	278.887680	41.733
H_2CO	$3_{0,3}$–$2_{0,2}$	218.222195	7.286[a]
	$3_{2,2}$–$2_{2,1}$	218.475642	40.040[a]
	$3_{2,1}$–$2_{2,0}$	218.760071	40.043[a]
N_2H^+	3–2	279.511760	9.324
OCS	18–17	218.903357	62.070
	23–22	279.685318	102.634
SO_2	$18_{1,17}$–$17_{2,16}$	288.519996	103.712

Note. [a] Observed earlier at the SMA in S255N by Cyganowski et al. (2007).

particularly focus on several key species, including N_2H^+, NH_3, deuterated molecules, SiO, methanol, etc. It is worth noting that we did not detect some important lines in our band, in particular, N_2D^+ and radio recombination lines.

We present the results in the form of maps as well as spectra and line parameters at selected positions. For continuum observations we give positions, flux densities, and size estimates of the continuum sources. In general the results are presented separately for the S255IR and S255N areas.

3.1. Millimeter Wave Continuum

Maps of the S255IR and S255N areas in 1.1 mm continuum overlaid on NIR *K*-band images (Ojha et al. 2011) are shown in Figure 1. The two brightest continuum sources visible in the S255IR map have been reported and discussed by Wang et al. (2011) (S255IR-SMA1 and S255IR-SMA2 in their nomenclature). In addition, they identified the S255IR-SMA3 clump which is indistinguishable from S255IR-SMA1 in our data (due to our lower angular resolution). On the other hand, our map shows an additional, very bright clump about 10″ further south. We designate this clump as S255IR-SMA4.

In the S255N area, in addition to the continuum clumps reported earlier (Cyganowski et al. 2007; Wang et al. 2011) our 1.1 mm continuum map shows three new features that are also detected in molecular emission (see below). We designate these as S255N-SMA4, SMA5, and SMA6; their parameters are given in Table 2.

3.2. Molecular Emission

Our data show that the intensity distributions for many molecular species are quite different from the continuum maps. In many cases, the molecular emission peaks do not coincide with the continuum peaks and there is also molecular emission without corresponding continuum emission. Below we describe in more detail the emission features of several key species.

Table 2
Positions, Flux Densities, Deconvolved Angular Sizes, and Position Angles of the Millimeter Wave Continuum Sources at 284 GHz as well as Flux Densities at 225 GHz (The Last Column) Measured with the SMA

Name	α(2000) (h m s)	δ(2000) (° ′ ″)	S_{284} (Jy)	θ_{max} (″)	θ_{min} (″)	P.A. (°)	S_{225} (Jy)
S255IR-SMA1	6:12:53.98	17:59:23.1	0.45	1.5	0.7	−14	0.29
S255IR-SMA2	6:12:53.75	17:59:25.7	0.43	2.9	2.2	11	0.30
S255IR-SMA4	6:12:54.03	17:59:11.5	0.31	4.4	3.5	−50	0.08
S255N-SMA1	6:12:53.64	18:00:26.8	0.75	3.0	2.0	−4	0.54
S255N-SMA2	6:12:52.95	18:00:31.7	0.05	2.5	2.1	−10	0.06
S255N-SMA3	6:12:53.62	18:00:18.7	0.05	3.3	2.9	−31	<0.03
S255N-SMA4	6:12:54.32	18:00:41.0	0.16	3.8	0.7	−12	0.04
S255N-SMA5	6:12:54.00	18:00:13.2	0.15	4.5	3.5	49	0.04
S255N-SMA6	6:12:53.04	18:00:03.4	0.14	7.9	1.3	−40	<0.03

3.2.1. NH_3

The ammonia emission in the S255IR area is rather weak (in accordance with Zinchenko et al. 1997) and shows significantly different distributions in the NH_3 (1,1) and (2,2) transitions (Figure 2). The (1,1) emission peaks at the SMA2 clump while the (2,2) emission peak coincides with SMA1. This indicates that the temperature of the SMA1 clump is much higher than that of SMA2. Indeed, Wang et al. (2011) derived a kinetic temperature of 150 K for SMA1, based on CH_3CN data, implying the presence of a hot core. The main emission peak toward SMA1 is observed at $V_{LSR} \approx 4.8$ km s^{-1}. There is a hint on another peak at $V_{LSR} \approx 9$ km s^{-1}.

The ammonia emission is relatively strong in S255N. In both the (1,1) and (2,2) transitions it extends far to the north from the main continuum clump (Figure 3). This extension has no counterpart in the continuum (at any observed wavelength) and almost no counterpart in other molecular lines (only N_2H^+ and perhaps DCO^+ show similar features, although less extended—see below). The (1,1) and (2,2) distributions in this northern extension are somewhat different; we discuss this in Section 4. We shall designate this northern source of ammonia emission as S255N-NH_3. The (1,1) and (2,2) spectra from this area are presented in Figure 4. They clearly show two narrow (line widths of about 1 km s^{-1}) velocity components (at approximately 10.1 and 8.2 km s^{-1}). The two velocity components have significantly different line ratios [$I(2,2)/I(1,1) \sim 0.2$ and ∼0.4 for the 8 and 10 km s^{-1} components, respectively], implying different temperatures for these two kinematic components. The temperature estimates are given in Section 4.

Another peak of ammonia emission—the strongest one in the (2,2) transition—is displaced a few arcseconds to the south from the main continuum source. Only the 10 km s^{-1} kinematic component is readily seen here, although there is a hint on the presence of the 8 km s^{-1} component in the (2,2) line (at about 1.5σ level). If real, it would imply a significant increase of the temperature of this component in this area since the $I(2,2)/I(1,1)$ ratio appears to be $\gtrsim 1$.

3.2.2. N_2H^+

N_2H^+ $J = 3$–2 emission is quite strong in both S255IR and S255N. The integrated intensity maps are shown in Figures 2 and 3. To better characterize the structure and kinematics of

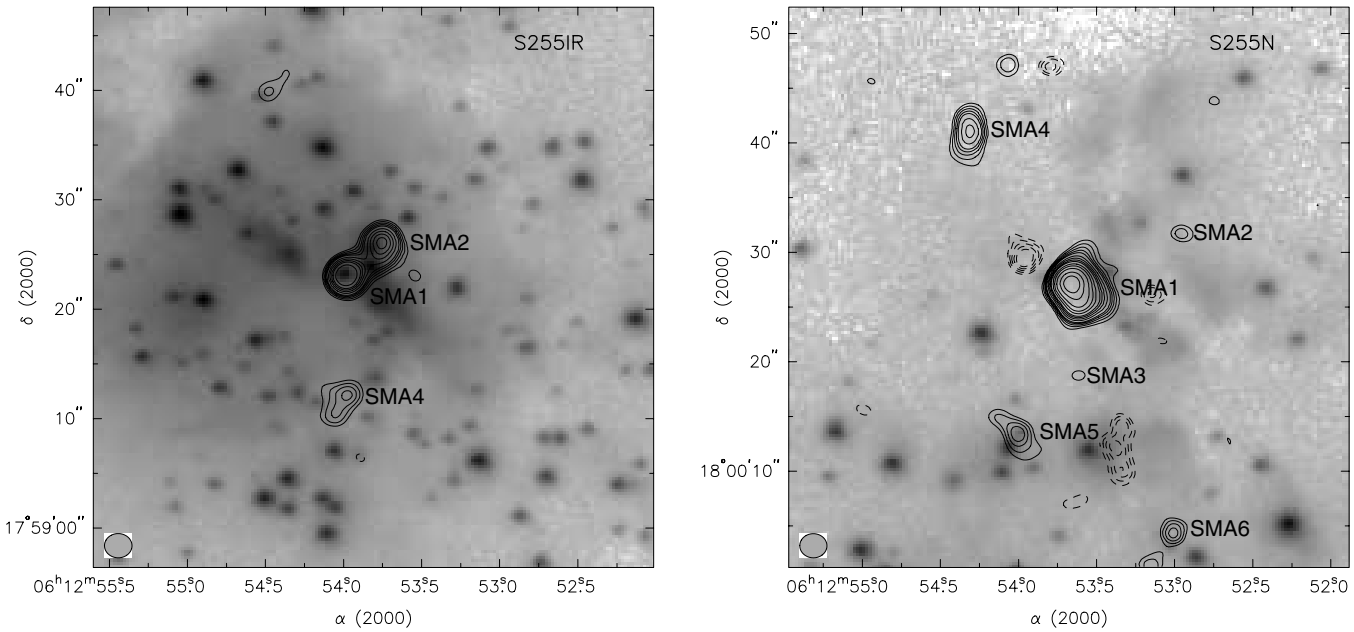

Figure 1. Maps of the 1.1 mm continuum emission in the S255IR (left panel) and S255N (right panel) areas (contours) overlaid on the *K*-band NIR images (in logarithmic scale) from Ojha et al. (2011). The contour levels are (2, 2.5, 3, 3.5, 4, 5, 6, 7, 8, 10) × 25 mJy beam^{-1} for S255IR and (−4, −3.5, −3, −2.5, −2, 2, 2.5, 3, 3.5, 4, 5, 6, 7, 8, 10, 12, 15, 20, 25) × 12.5 mJy beam^{-1} for S255N. The dashed contours show negative features due to the missing flux. The SMA beam is shown in the lower left corner of both panels.

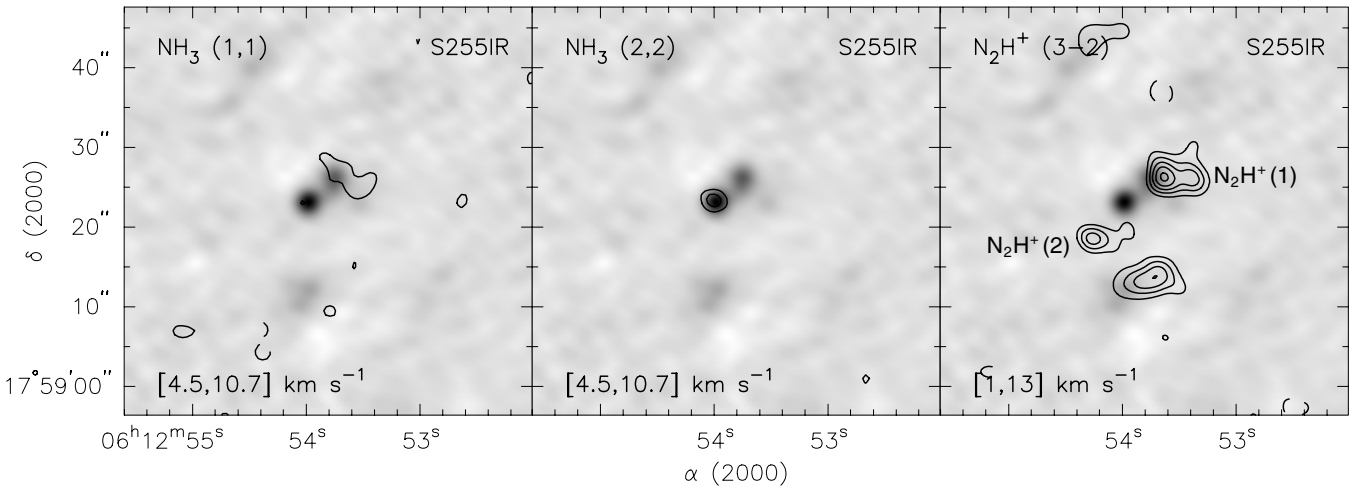

Figure 2. Maps of the NH_3 (1,1), NH_3 (2,2), and N_2H^+ (3–2) integrated line emission in the S255IR area (contours) overlaid on the 1.1 mm continuum image. The velocity ranges are indicated at the bottom of the plots. The contour levels are (−3, 3, 5, 7) × 10 mJy beam^{-1} km s^{-1} for NH_3 and (−3, 3, 5, 7, 9, 11) × 1.4 Jy beam^{-1} km s^{-1} for N_2H^+. The dashed contours show negative features due to the missing flux.

these regions, we present in Figures 5 and 6 the channel maps of this line with 2 km s^{-1} resolution.

In S255IR, while there is no detectable N_2H^+ emission directly associated with the SMA1 clump, several N_2H^+ emission peaks can be seen in this general area (Figure 2). Two of these are related to the SMA2 and SMA4 clumps, although the N_2H^+ peaks do not coincide exactly with the continuum peaks. Two other peaks have no associated continuum. One of these is seen as an extension to the west from the SMA2 clump and is apparently related to the CH_3OH emission feature noticed by Wang et al. (2011). This feature is seen in several other methanol lines in our data. NH_3 (1,1) emission is also observed here, as are some other lines (e.g., H_2CO). We shall designate this source as S255IR-N_2H^+(1). Another quite strong N_2H^+ peak, shifted to the SE from SMA1, has no counterpart in the continuum or in any observed lines. For this emission feature we shall use the name S255IR-N_2H^+(2). Both features are marked in Figure 2.

In the S255N area, the N_2H^+ emission shows an extension in the same direction as NH_3 (Figure 3). The main peak of the N_2H^+ emission is displaced from the continuum peak (similar to the ammonia) and has an extension roughly in the direction of the outflow described by Wang et al. (2011). There is one more N_2H^+ emission peak about 25″ to the SSW from S255N-SMA1; it is associated with weak continuum emission (S255N-SMA6) and is traced by several other molecular lines (see below). The spectra of N_2H^+ and other molecules from S255N-SMA1 are shown in Figure 7.

3.2.3. DCN, DNC, and DCO$^+$

Our data set contains lines of several deuterated molecules: DCN J = 3–2 and J = 4–3, DNC J = 3–2, and DCO^+ J = 4–3. DCN emission is quite strong in both S255IR and S255N. In S255IR it is observed in both main clumps, SMA1

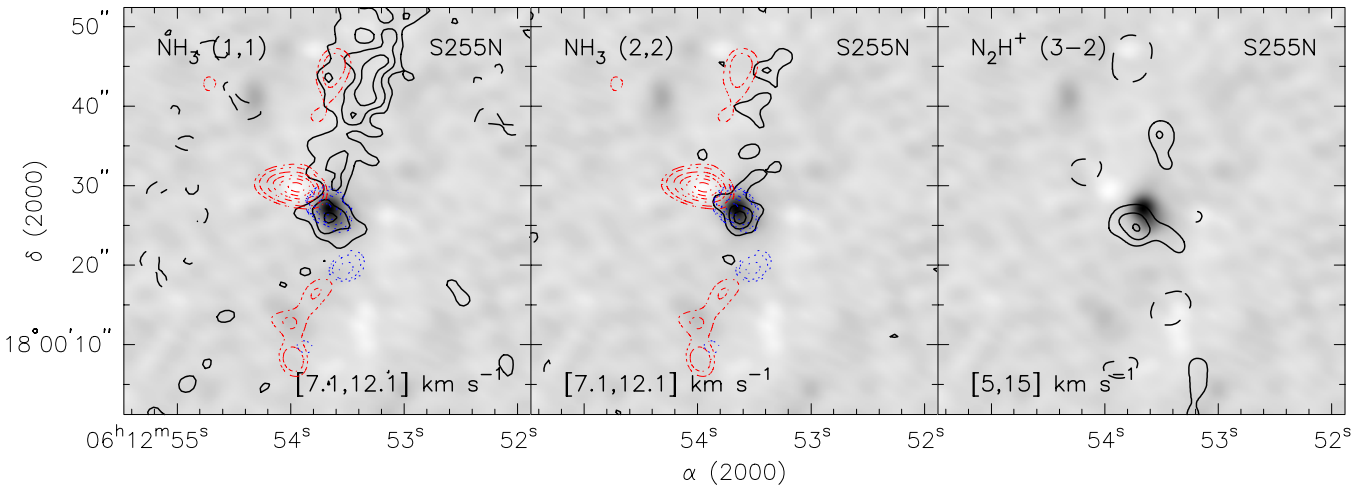

Figure 3. Maps of the NH_3 (1,1), NH_3 (2,2), and N_2H^+ (3–2) integrated line emission in the S255N area (contours) overlaid on the 1.1 mm continuum image. The velocity ranges are indicated at the bottom of the plots. The contour levels are $(-3, 3, 5, 7) \times 10$ mJy beam^{-1} km s^{-1} for NH_3 and $(-3, 3, 5, 7) \times 1.4$ Jy beam^{-1} km s^{-1} for N_2H^+. The dashed contours show negative features due to the missing flux. The dash-dotted (red in the online version) and dotted (blue in the online version) contours show the redshifted and blueshifted high-velocity CO emission, respectively.

(A color version of this figure is available in the online journal.)

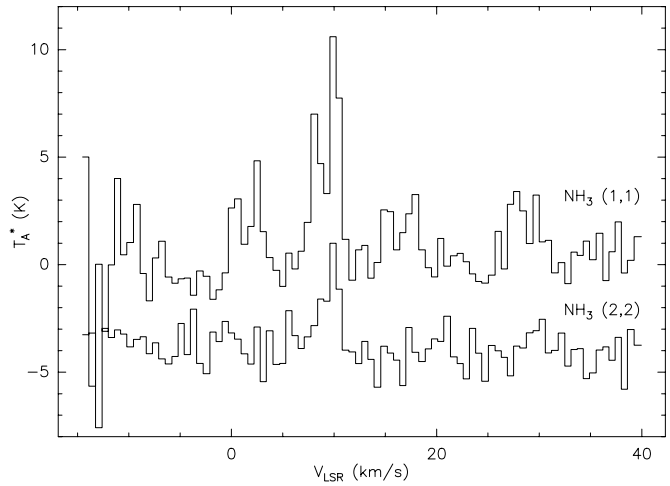

Figure 4. Spectra of the NH_3 (1,1) and (2,2) emission from the S255N-NH_3 area averaged over the region $2\farcs5 \times 3\farcs5$ centered at R.A.(2000) = $06^h12^m53\fs39$, decl.(2000) = $18°00'41\farcs0$ (in units of brightness temperature—the conversion factor is approximately 320 K per Jy beam^{-1}). The (2,2) spectrum is shifted by −4 K along the vertical axis for clarity.

and SMA2, although its peak is shifted from the continuum peak in SMA1 (Figure 8). The DCN $J = 4$–3 line is also seen in SMA4. In S255N the DCN emission coincides with the SMA1 continuum clump, having an extension to the north (Figure 9).

The DNC emission is significantly weaker than DCN. We did not detect DNC in the S255IR area. In S255N it is detected, but the peak is shifted from the DCN and continuum peaks.

DCO^+ emission is seen in both areas. Its distribution is significantly different from that of DCN, and qualitatively resembles that of N_2H^+. In particular, both species avoid ionized regions, and both are observed toward the S255N-SMA6 clump (in contrast to most other molecules).

3.2.4. SiO

As expected, the bulk of the SiO emission in both S255IR and S255N (Figures 10 and 11) is apparently associated with outflows. In S255IR the strongest SiO emission is observed toward the SMA1 clump (Figure 10) which is probably the driving source of the outflow (Wang et al. 2011). The peak is shifted from the continuum peak in the direction of the redshifted outflow lobe. The central velocity is significantly higher than for most of the other lines (Figure 7). There is also blueshifted high-velocity SiO emission. A discussion of the high-velocity emission in various lines is given in Section 4.

S255IR also shows narrow-line SiO emission near SMA2 and SMA4. The possible association of this emission with other features is discussed below. The details of SiO kinematics can be seen in Figure 12. In particular we see SiO emission from the blueshifted lobe of the extended outflow described by Wang et al. (2011). However, there is no SiO emission from the redshifted lobe of this outflow.

In S255N (Figure 11) the main peak of the SiO emission coincides with the SW (blueshifted) lobe of the molecular outflow traced in CO (Wang et al. 2011) and other lines. The SiO profile shows an extended blue wing. In addition, there are very broad SiO emission features clearly seen in the SiO channel maps (Figure 13) associated with the SMA3 and SMA5 clumps. In the vicinity of the SMA3 clump, the SiO emission spans from about −45 km s^{-1} to about +65 km s^{-1} (Figure 14). The blueshifted and redshifted parts of the emission are spatially separated as can be easily seen in the channel maps (Figure 13) and more clearly in Figure 15. All this indicates the presence of a high-velocity outflow associated with this clump. This outflow is also traced in high-velocity CO emission (Figure 3 here and Figure 10 in Wang et al. 2011).

The total width of the SiO emission associated with the SMA5 clump is about 50 km s^{-1} (Figure 16). The blueshifted and redshifted SiO emissions are spatially separated (Figure 17). This suggests that another outflow is related to this clump. The driving source of the outflow is shifted by a few arcseconds to the south from the SMA5 continuum peak.

3.2.5. CH_3OH

In our band we observed several methanol lines of different excitation. Maps of the methanol emission in the lines detected in the S255IR and S255N areas are presented in Figures 18 and 19.

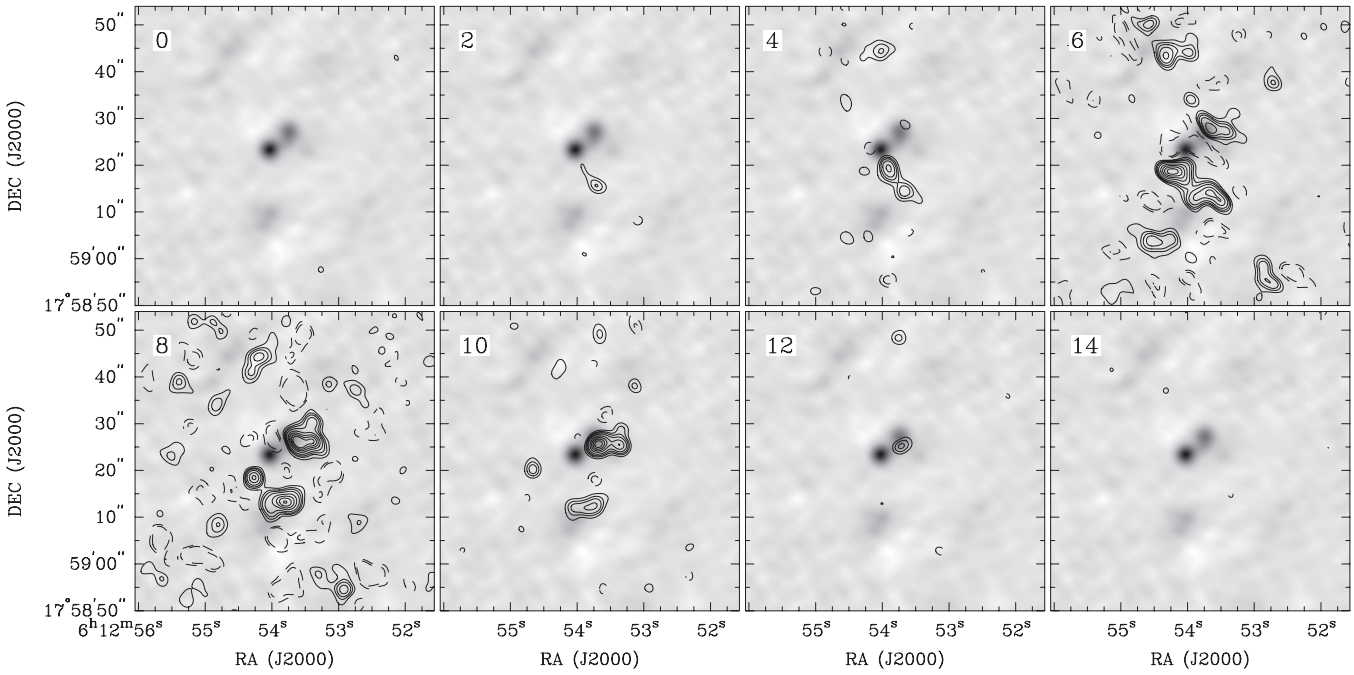

Figure 5. Channel maps of the N_2H^+ (3–2) line emission in the S255IR area (contours) overlaid on the 1.1 mm continuum image. The numbers in the upper left corner indicate the channel velocity in km s^{-1}. The contour levels are (−5, −3, 3, 5, 7, 10, 15, 20) × 100 mJy beam^{-1}. The dashed contours show negative features due to the missing flux. The maps at the central velocities (6–10 km s^{-1}) may show spurious features due to a limited dynamical range of the observations.

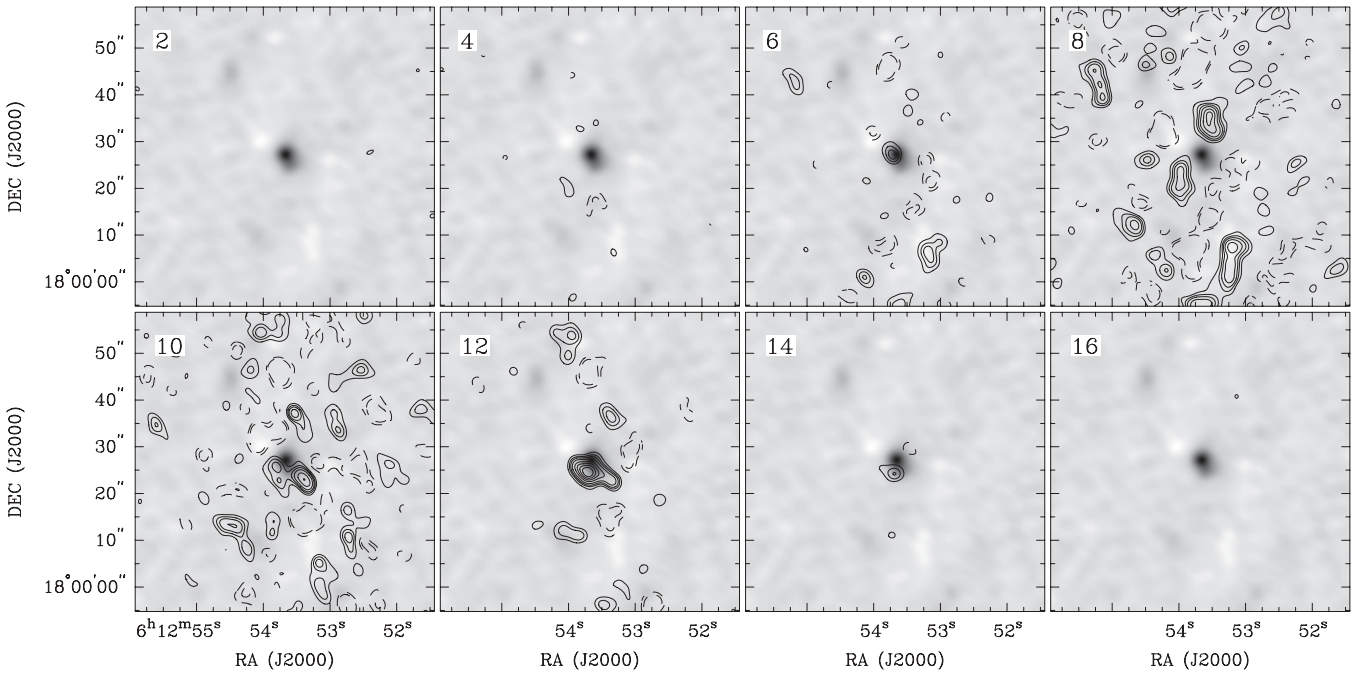

Figure 6. Channel maps of the N_2H^+ (3–2) line emission in the S255N area (contours) overlaid on the 1.1 mm continuum image. The numbers in the upper left corner indicate the channel velocity in km s^{-1}. The contour levels are (−5, −3, 3, 5, 7, 10, 15, 20) × 100 mJy beam^{-1}. The dashed contours show negative features due to the missing flux. The maps at the central velocities (6–10 km s^{-1}) may show spurious features due to a limited dynamical range of the observations.

The main features of the methanol emission in the central parts of S255IR and S255N are the same as reported by Wang et al. (2011). The highest excitation lines are detected only in S255IR-SMA1. Several methanol lines trace some of our new continuum clumps, in particular S255IR-SMA4, S255N-SMA4, and S255N-SMA5. Wang et al. (2011) reported an emission in one of the methanol lines from the area which we designate here as S255IR-N_2H^+(1). Our data show an emission here in three other methanol lines.

Methanol lines from S255IR-SMA1 and S255N-SMA1 show wings, although less extended than in SiO. We do not see high velocity methanol emission from S255N-SMA3 and SMA5 where we report SiO outflows.

An inspection of the presented maps indicates apparent peculiarities in the methanol excitation. For example, the low excitation 5_1–4_2 E line is much stronger in S255-SMA1 than in SMA2, in contrast to other lines of comparable excitation. The same can be said about the 9_{-1}–8_0 E line in the S255N area

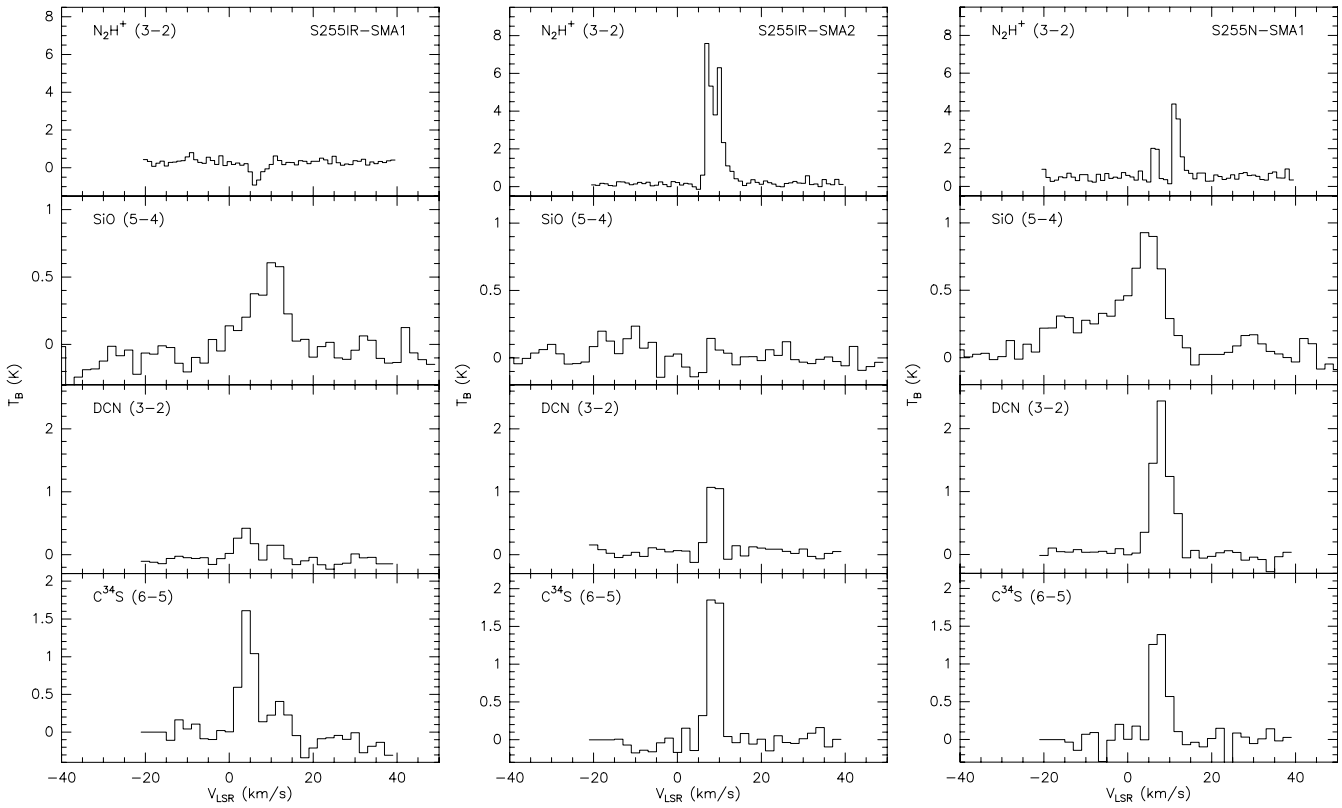

Figure 7. Spectra of the N_2H^+ $J = 3$–2, SiO $J = 5$–4, DCN $J = 3$–2, and $C^{34}S$ $J = 6$–5 emission averaged over the regions $2''.5 \times 2''.5$ centered at S255IR-SMA1, S255IR-SMA2, and S255N-SMA1 (in units of brightness temperature).

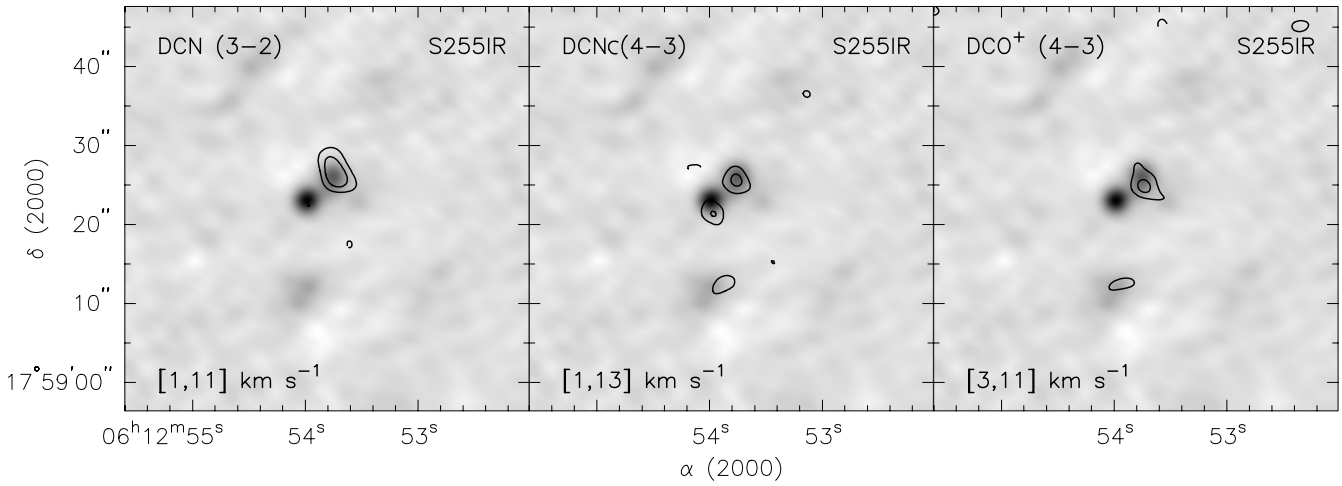

Figure 8. Maps of the DCN $J = 3$–2 and $J = 4$–3, and DCO^+ $J = 4$–3 integrated line emission in the S255IR area (contours) overlaid on the 1.1 mm continuum image. The velocity ranges are indicated at the bottom of the plots. The contour levels are $(-3, 3, 5) \times 0.4$ Jy beam^{-1} km s^{-1} for DCN $J = 3$–2 and DCO^+ $J = 4$–3, and $(-3, 3, 5) \times 0.55$ Jy beam^{-1} km s^{-1} for DCN $J = 4$–3. The dashed contours show negative features due to the missing flux.

(the component shifted by a few arcseconds to northeast from S255N-SMA1). These and some other methanol lines in our band can be masing (Sobolev 1993; Cragg et al. 2005; Voronkov et al. 2012; A. Sobolev 2012, private communication).

3.2.6. Other Lines

Our data set contains several other important molecular lines including $C^{34}S$, HC_3N, SO, SO_2, H_2CO, H_2CS, CH_3CN, OCS, and HNCO. Most of them have not been observed with high angular resolution in both these objects before now. Some of these lines, in particular those with relatively high excitation energy (e.g., HC_3N and SO_2), are detected almost exclusively toward the hot core in S255IR-SMA1. Other molecules (e.g., SO) trace the outflows. In Figures 10, 11, 20, and 21 we present maps of the emission of $C^{34}S$, HC_3N, H_2CO, H_2CS, and SO_2. In particular, fairly strong emission is observed in H_2CO. It traces most of the new continuum clumps in both S255IR and S255N, and also several other features, including S255IR-N_2H^+(1).

It is worth noting that our $C^{34}S$ $J = 6$–5 map of the S255IR area looks very different from the ^{13}CS $J = 5$–4 map presented by Wang et al. (2011). Our data show that the $C^{34}S$ emission is of similar intensity in both S255IR-SMA1 and S255IR-SMA2, and approximately coincident with the dust continuum peaks (Figures 7 and 10). The ^{13}CS emission of Wang et al. (2011)

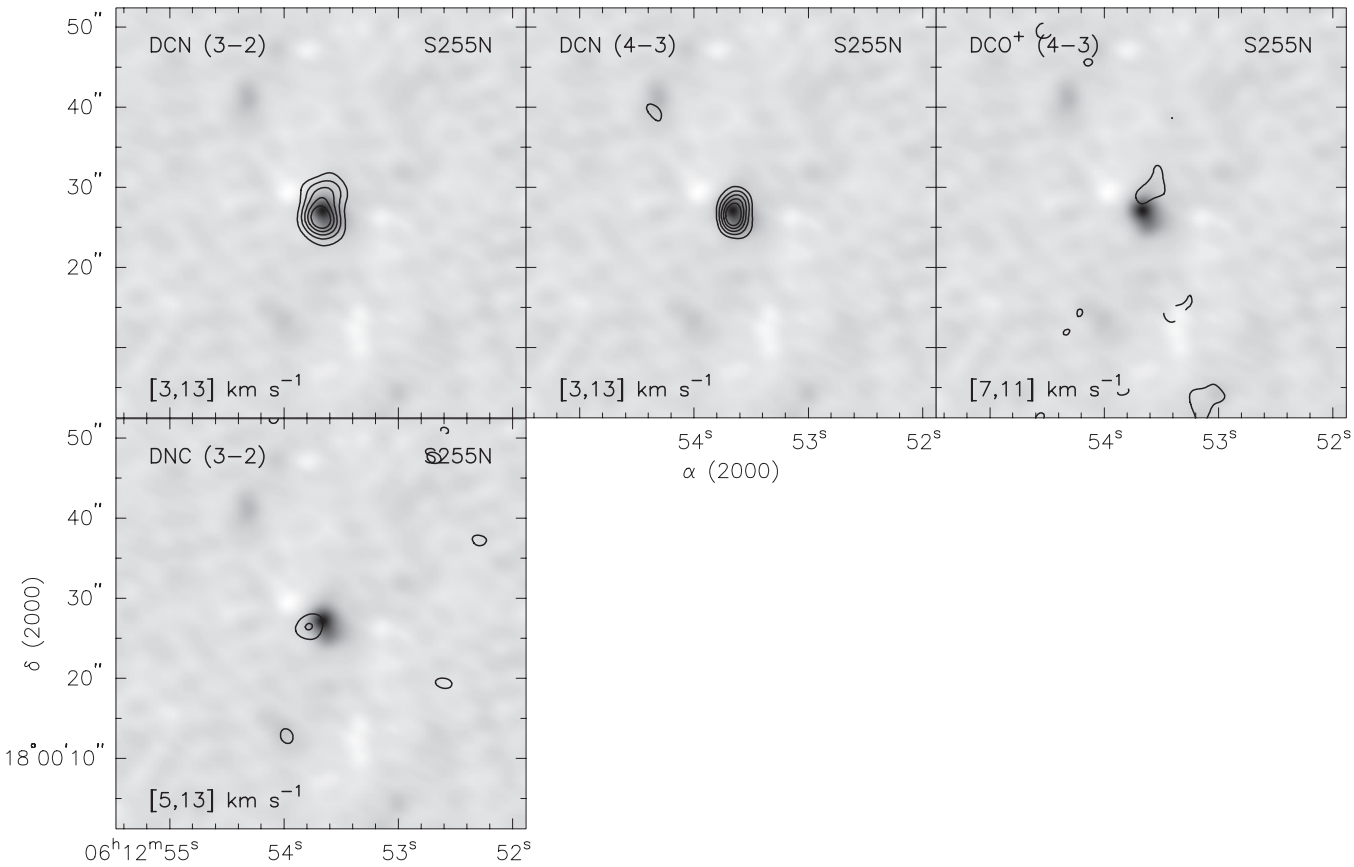

Figure 9. Maps of the DCN $J = 3$–2 and $J = 4$–3, DNC $J = 3$–2 and DCO^+ $J = 4$–3 integrated line emission in the S255N area (contours) overlaid on the 1.1 mm continuum image. The velocity ranges are indicated at the bottom of the plots. The contour levels are $(-3, 3, 5, 7, 9, 11) \times 0.5$ Jy beam^{-1} km s^{-1} for DCN $J = 3$–2, $(-3, 3, 5, 7, 9, 11) \times 0.6$ Jy beam^{-1} km s^{-1} for DCN $J = 4$–3, and $(-3, 3, 5) \times 0.25$ Jy beam^{-1} km s^{-1} for DNC $J = 3$–2 and DCO^+ $J = 4$–3. The dashed contours show negative features due to the missing flux.

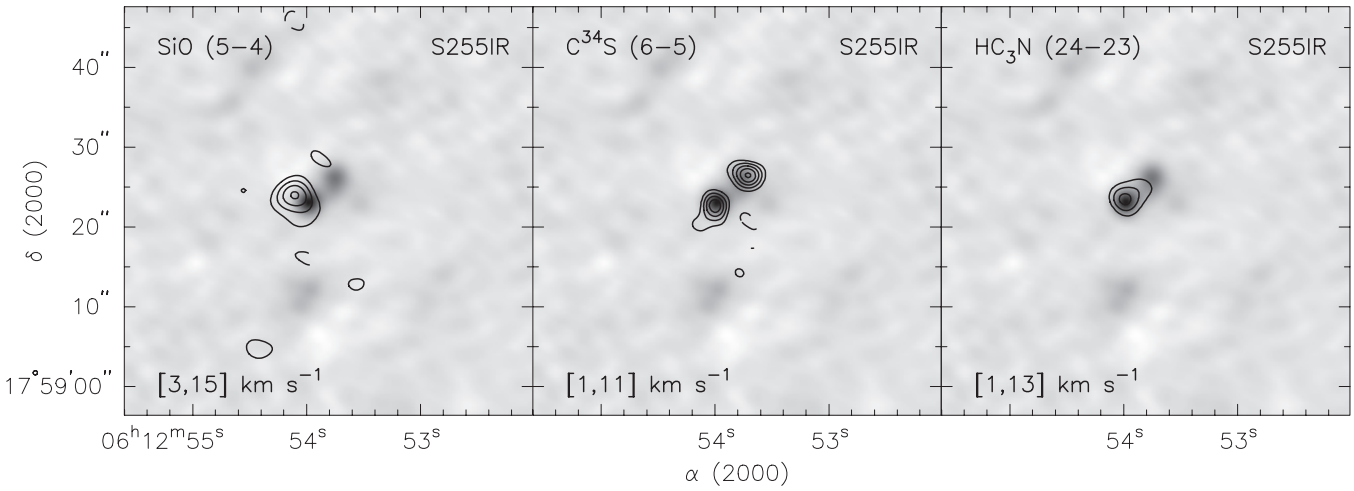

Figure 10. Maps of the SiO $J = 5$–4, $C^{34}S$ $J = 6$–5, and HC_3N $J = 24$–23 integrated line emission in the S255IR area (contours) overlaid on the 1.1 mm continuum image. The velocity ranges are indicated at the bottom of the plots. The contour levels are $(-3, 3, 5, 7, 9) \times 0.4$ Jy beam^{-1} km s^{-1} for SiO $J = 5$–4 and HC_3N $J = 24$–23, and $(-3, 3, 5, 7) \times 0.55$ Jy beam^{-1} km s^{-1} for $C^{34}S$ $J = 6$–5. The dashed contours show negative features due to the missing flux.

is seen only in S255IR-SMA1 and is significantly shifted from the continuum peak. Interestingly, our ^{13}CS observations of the same line show the intensity distribution very similar to $C^{34}S$ $J = 6$–5. The only reasonable explanation is that the bulk of the ^{13}CS emission is resolved out by the smaller beam of Wang et al. (2011; which is about two times narrower than our beam), and they see only a compact structure at the eastern edge of S255IR-SMA1.

3.3. Decimeter and Centimeter Wave Radio Continuum Emission

In Figure 22 we show a large-scale 610 MHz map of the region, obtained with the GMRT. It covers the evolved H II regions S255, S256, and S257. Two compact sources in the center are associated with the S255IR and S255N star-forming cores.

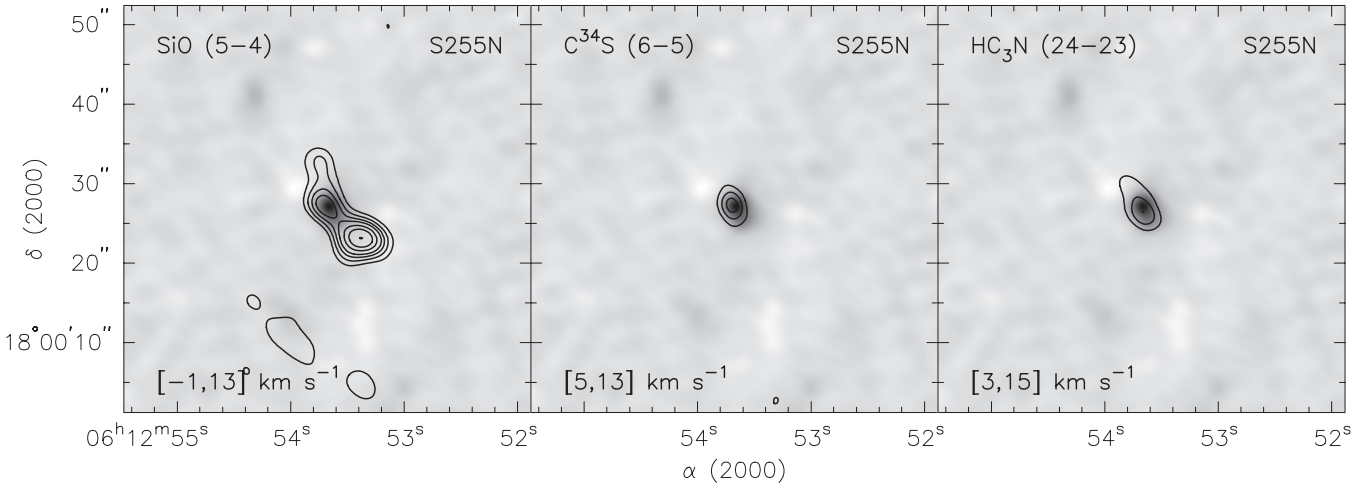

Figure 11. Maps of the SiO $J = 5$–4, $C^{34}S$ $J = 6$–5, and HC_3N $J = 24$–23 integrated line emission in the S255N area (contours) overlaid on the 1.1 mm continuum image. The velocity ranges are indicated at the bottom of the plots. The contour levels are $(-3, 3, 5, 7, 9, 12, 15, 19) \times 0.4$ Jy beam^{-1} km s^{-1} for SiO $J = 5$–4, $(-3, 3, 5, 7) \times 0.55$ Jy beam^{-1} km s^{-1} for $C^{34}S$ $J = 6$–5, and $(-3, 3, 5, 7) \times 0.4$ Jy beam^{-1} km s^{-1} for HC_3N $J = 24$–23. The dashed contours show negative features due to the missing flux.

Table 3
Results of the GMRT Radio Continuum Measurements

Name	S_{1280} (mJy)	θ_{max} ($''$)	θ_{min} ($''$)	P.A. ($^\circ$)	S_{610} (mJy)
S255-2a	3.81 ± 0.49	8.1	7.0	46.4	4.22 ± 0.86
S255-2b	1.53 ± 0.41	7.7	3.8	55.9	0.96 ± 0.31
S255-2c	1.11 ± 0.32	7.7	4.3	58.9	<0.4
S255-1	20.25 ± 0.46	10.5	5.0	61.1	10.48 ± 0.78

Note. The fluxes, sizes (convolved), and position angles at 1280 MHz as well as fluxes at 610 MHz are indicated.

In Figure 23, we present 1280 MHz GMRT continuum maps of S255IR and S255N. A comparison of the original GMRT maps with high-frequency VLA archival maps (in particular, at 15 GHz) shows a positional shift of a few arcseconds between the maps. The reasons for this shift are unclear but probably are related to phase calibration at the GMRT. We made positional corrections to the GMRT maps to compensate for the shifts. Thus, the absolute coordinates in these maps are not reliable to more than a few arcseconds.

The main components seen in the GMRT maps were identified by Snell & Bally (1986) and we follow their nomenclature here for the radio continuum sources (in particular S255-1 corresponds to S255N). Our data extend the frequency range of radio continuum observations and provide important information on the structure of the radio continuum sources at low frequencies. In our 610 MHz map, we only see emission from the sources S255-2a and S255-2b in the S255-IR cluster. These two sources are not resolved in the 610 MHz map, however, they appear as two distinct sources in our higher resolution 1280 MHz map. We measured flux densities and sizes of the radio continuum sources using a two-dimensional elliptical Gaussian model via the AIPS task JMFIT; the results are given in Table 3. In Section 4, we compare our data with observations at other wavelengths and discuss possible relations between the radio continuum and molecular emission.

Although at the VLA only spectral line observations were made we combined line-free channels to form continuum images at 23.7 GHz. These continuum maps are not of very high quality (the usable bandwidth was only about 3 MHz) and so the detection level and uncertainties just are not that good. We detected S255-1 and S255-2c. Their measured fluxes are 19 ± 2 mJy and 3.3 ± 0.5 mJy, respectively. S255-2a and 2b are not detected.

4. DISCUSSION

4.1. General Morphology and Kinematics

Our data indicate the presence of several new clumps in the mapped areas. Some of them are visible in the 1.1 mm continuum map. Most of these continuum clumps also show molecular emission (although the sets of emitting lines are somewhat different for each one). A comparison with our recent NIR *J*-, *H*-, and *K*-band observations of this area (Ojha et al. 2011) shows almost no association of the newly detected continuum clumps with the NIR sources (Figure 1). This implies that these clumps are at a very early stage of evolution.

A pronounced example is the new clump which we designate as SMA4 in the S255IR area. It shows fairly strong continuum emission (Table 2) and is associated with emission in many molecular lines including N_2H^+, DCO^+, DCN, H_2CO, H_2CS, and CH_3OH. Interestingly, emission peaks of different species are located at different distances from the continuum source, implying a chemical abundance gradient in approximately the east–northeast direction (Figure 24). There is also a moderate velocity gradient in this direction that can be seen in the N_2H^+ line channel maps (Figure 5) and is also illustrated by the position–velocity diagram in Figure 25. The total velocity change is about 5 km s^{-1}. One of the SiO clumps, partly overlapping with the N_2H^+ emission, also appears to be associated with this object, being located at the largest distance from the continuum source ($\sim 7''$; Figures 2, 5, 10, and 12). At the same time the $C^{18}O$ emission is very weak. Perhaps we see here an outflow oriented almost perpendicular to the line of sight. This can explain the relatively small velocity gradient and narrow line widths.

The data also show a complex kinematics of some of the previously known clumps. As mentioned above the ammonia lines probably have two velocity components in S255IR-SMA1 and S255N-SMA1. Wang et al. (2011) also mentioned that the $C^{18}O$ spectrum toward S255IR-SMA1 shows two peaks. The

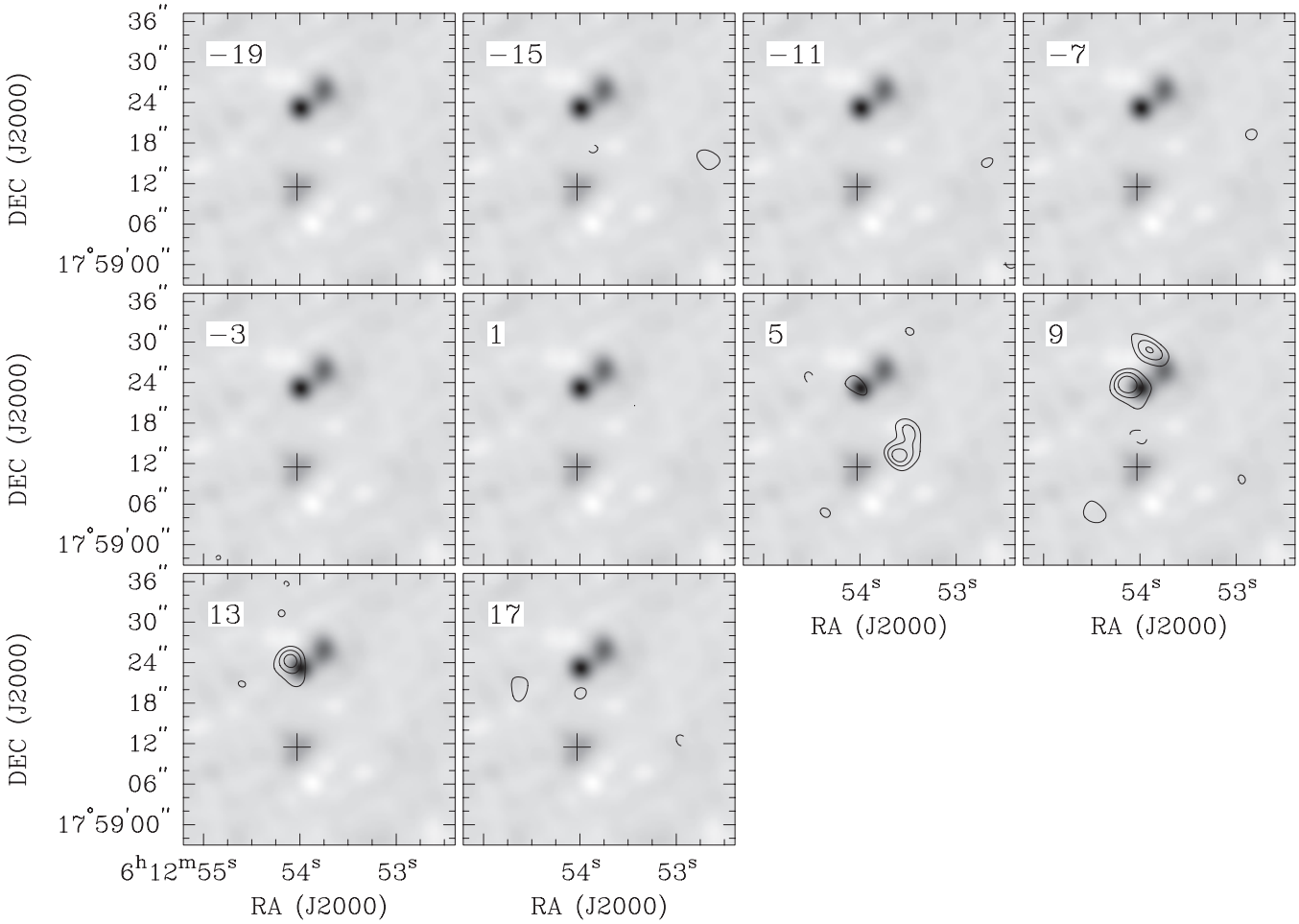

Figure 12. Channel maps of the SiO (5–4) line emission in the S255IR area (contours) overlaid on the 1.1 mm continuum image. The numbers in the upper left corner indicate the channel velocity in km s^{-1}. The contour levels are (−3, 3, 5, 7, 10, 15, 20) × 45 mJy beam^{-1}. The dashed contours show negative features due to the missing flux. The cross marks the position of the SMA4 continuum clump.

presence of two velocity components is also evident in the spectra shown in Figure 7. The most intense emission toward S255IR-SMA1 in various lines including the highest excitation lines is observed at $V_{\rm LSR} \sim$ 4–5 km s^{-1}. Another component at $V_{\rm LSR} \sim$ 10 km s^{-1} is seen in lines of lower excitation and has a somewhat smaller line width.

In S255N-SMA1 the data also show two kinematic components—at $V_{\rm LSR} \sim$ 8 and ∼10 km s^{-1}. The lines with the excitation energy $E_{\rm u} \gtrsim$ 40 K are observed at $V_{\rm LSR} \sim$ 8 km s^{-1} while lower excitation lines have emission peaks in the range $V_{\rm LSR} \sim$ 8–10 km s^{-1}.

4.2. Basic Physical Parameters of the Clumps

4.2.1. Kinetic Temperature

We derive gas kinetic temperature from our ammonia observations using the usual approach described for example in Mangum et al. (1992) and Harju et al. (1993). The NH_3 (1,1) and (2,2) spectra were fitted using the GILDAS software package (http://www.iram.fr/IRAMFR/GILDAS). Results of the temperature estimates for the continuum clumps are given in Table 4. Typical uncertainties are 20%–30%. As mentioned above, in S255IR-SMA1 and S255N-SMA1 we probably see secondary velocity components. The signal-to-noise ratios for them are very low; we show estimates of the kinetic temperature for these components in parenthesis with question marks.

In S255N-NH_3 we obtained the temperature of about 13 K for the 8 km s^{-1} component and about 23 K for the 10 km s^{-1} component. The temperature of the latter component is practically the same in S255N-NH_3 and in S255N-SMA1, while the temperature of the 8 km s^{-1} component sharply increases toward S255N-SMA1 from very low values at S255N-NH_3. The temperature estimate for S255IR-N_2H^+(1) is about 50 K.

Our data set contains several methanol transitions of significantly different excitation. In principle they could be used for temperature estimates with the traditional method of rotational diagrams. Unfortunately in most cases the constructed rotational diagrams do not allow any reasonable temperature fit. The reason can be a significant deviation from LTE conditions assumed by the method of rotational diagrams. As mentioned above, several of the observed transitions may be masing. Preliminary results of non-LTE modeling based on the approach described in Salii & Sobolev (2006) and Sutton et al. (2004) show a fairly good agreement with the ammonia temperature estimates (S. Salii & A. Sobolev 2012, private communication). Thus, we use only these latter estimates here.

4.2.2. Masses and Densities

Here, we present some simple estimates of clump masses, sizes, and densities derived from the dust continuum emission. Our continuum flux measurements at two different frequencies (∼225 and ∼285 GHz) imply a spectral index of about 2 for

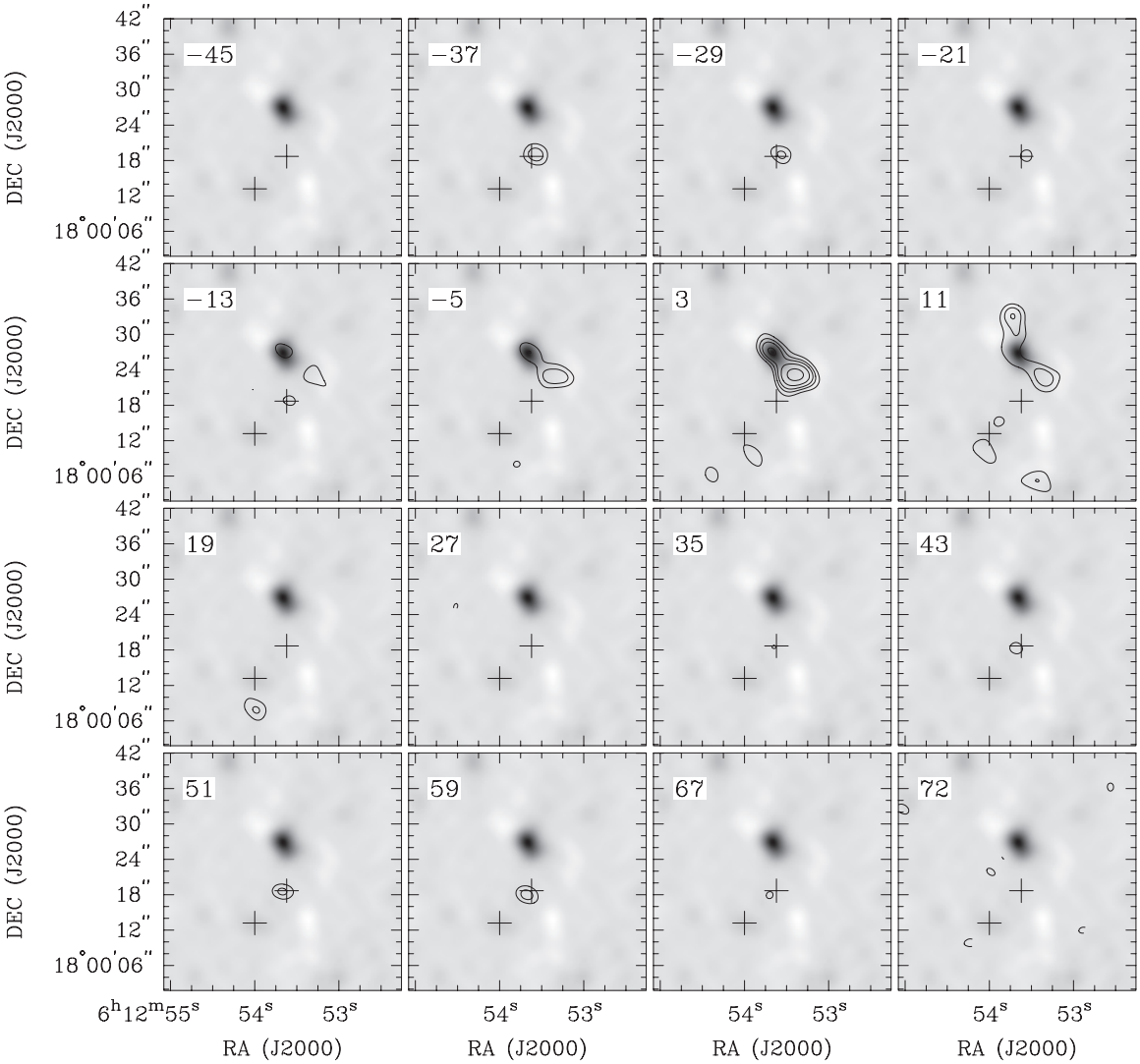

Figure 13. Channel maps of the SiO (5–4) line emission in the S255N area (contours) overlaid on the 1.1 mm continuum image. The numbers in the upper left corner indicate the channel velocity in km s^{-1}. The contour levels are (−3, 3, 5, 7, 10, 15, 20) × 40 mJy beam^{-1}. The dashed contours show negative features due to the missing flux. The crosses mark the positions of the SMA3 and SMA5 continuum clumps.

Table 4
Velocities and Physical Parameters (Line Width, Linear Size, Kinetic Temperature Derived from Ammonia Observations, *Assumed* Dust Temperature, Mass, Virial Mass, and Mean Density) of the Millimeter Wave Continuum Sources

Name	V_{LSR} (km s^{-1})	ΔV (km s^{-1})	L (pc)	$T_{kin}(NH_3)$ (K)	T_d[a] (K)	M ($M_\odot$)	M_{vir} ($M_\odot$)	$\bar{n}$ (cm^{-3})
S255IR-SMA1	4.4	3.3	0.012	240, (80 ?)	40	10	14	2×10^8
S255IR-SMA2	9.2	2.0	0.031	44	40	10	13	10^7
S255IR-SMA4	7.9	2.6	0.048	$\lesssim$20	20	14	34	4×10^6
S255N-SMA1	8.0	3.5	0.030	29, (>200 ?)	30	23	39	3×10^7
S255N-SMA2	8.7	3.0	0.028		20	2	26	4×10^6
S255N-SMA3	9.0	<2	0.037	29	30	2	<10	10^6
S255N-SMA4	7.0	4.2	0.020		20	8	40	2×10^7
S255N-SMA5	9.5	3.9	0.048	24	25	7	80	2×10^6
S255N-SMA6	8.9	4.5	0.039		20	6	80	4×10^6

Note. [a] Assumed.

both S255IR-SMA1 and SMA2. This indicates optically thick emission, which is unrealistic. A comparison of our measured flux densities at 225 GHz for SMA1 and SMA2 with those published by Wang et al. (2011) shows that our values are about two times higher. This could be caused by different uv ranges of the observations; with our lower resolution data we are less susceptible to missing flux. Our 285 GHz data have an angular resolution closer to that of Wang et al. (2011). Using our 285 GHz flux densities and the 225 GHz flux densities from Wang et al. (2011), we obtain a spectral index of about 4 for

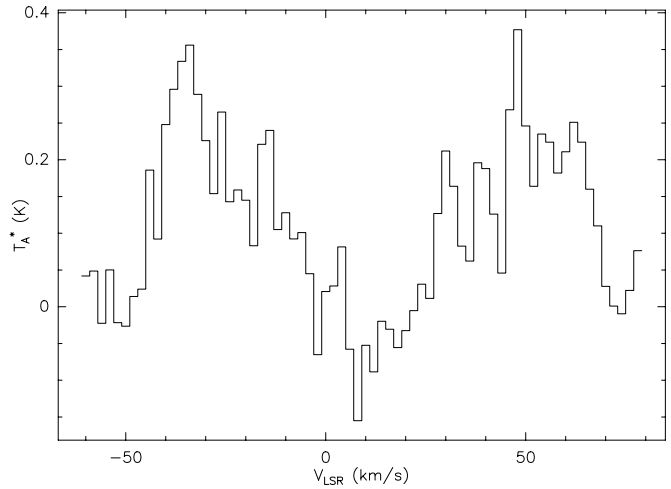

Figure 14. Spectrum of the SiO $J = 5$–4 emission from the S255N-SMA3 area averaged over the region $3\farcs5 \times 2\farcs5$ centered at S255N-SMA3 (in units of brightness temperature—the conversion factor is approximately 2.2 K per Jy beam^{-1}).

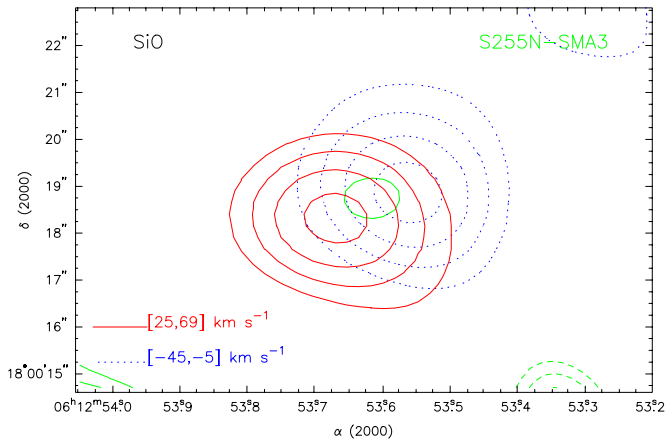

Figure 15. Maps of the blueshifted (blue thick dotted contours) and redshifted (red thick solid contours) SiO $J = 5$–4 emission in the S255N-SMA3 area overlaid with the map of the 1.1 mm continuum emission (green thin contours). The velocity ranges are indicated at the bottom of the plot. The contour levels for SiO are $(-3, 3, 5, 7, 9) \times 0.75$ Jy beam^{-1} km s^{-1}. The contour parameters for continuum are the same as in Figure 1. The dashed contours show negative features due to the missing flux.

(A color version of this figure is available in the online journal.)

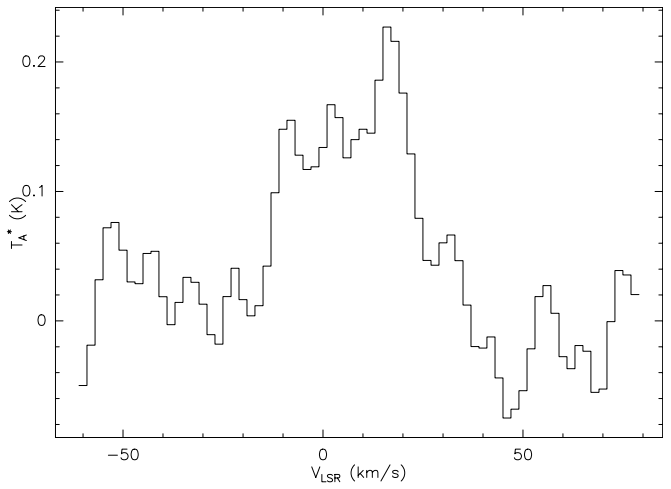

Figure 16. Spectrum of the SiO $J = 5$–4 emission from the S255N-SMA5 area averaged over the region $5\farcs5 \times 5\farcs5$ shifted to the south by $4\farcs7$ from the S255N-SMA5 central position (in units of brightness temperature—the conversion factor is approximately 2.2 K per Jy beam^{-1}).

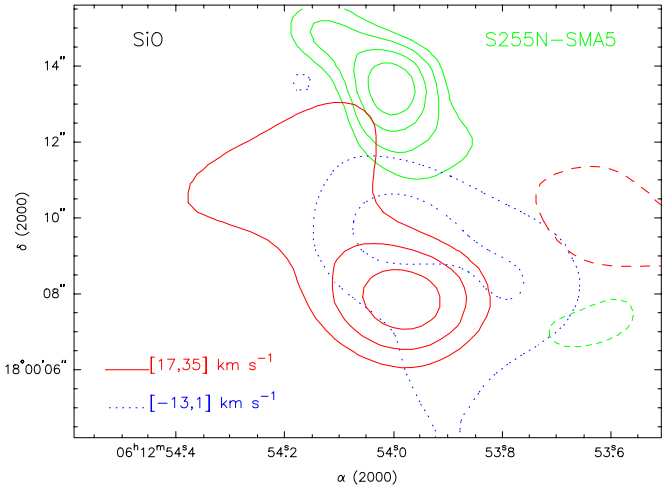

Figure 17. Maps of the blueshifted (blue thick dotted contours) and redshifted (red thick solid contours) SiO $J = 5$–4 emission in the S255N-SMA5 area overlaid with the map of the 1.1 mm continuum emission (green thin contours). The velocity ranges are indicated at the bottom of the plot. The contour levels for SiO are $(-3, 3, 5, 7) \times 0.25$ Jy beam^{-1} km s^{-1}. The contour parameters for continuum are the same as in Figure 1. The dashed contours show negative features due to the missing flux.

(A color version of this figure is available in the online journal.)

these clumps, as expected for optically thin dust emission. This shows that even simple mass estimates based on continuum flux densities are highly uncertain and strongly depend on the uv-coverage.

We assume the dust temperatures (T_d) close to the kinetic temperatures derived from the ammonia observations. For the clumps with no ammonia temperatures we assume $T_d = 20$ K. In S255IR-SMA1 and S255N-SMA1 we see components with different temperatures. For the bulk of the dust emission we assume the lowest temperature. In S255IR-SMA1 the ammonia emission is very weak and estimates of the lowest temperature are very uncertain. We assume $T_d = 40$ K in accordance with the value of kinetic temperature found in single-dish observations (Zinchenko et al. 2009). Then, we assume a gas-to-dust mass ratio of 100, and adopt a dust absorption efficiency following Ossenkopf & Henning (1994). The masses derived in this way are given in Table 4 and range from 2 to 34 $M_\odot$.

In this table, we also indicate velocities and typical line widths for the clumps as well as their linear sizes and virial masses. The velocities and line widths in most cases were derived from $C^{18}O$ and/or $C^{34}S$ spectra. In some clumps (S255IR-SMA4, S255N-SMA6), these lines are too weak and we used data of other lines, in particular N_2H^+ for S255N-SMA6 and H_2CO for S255IR-SMA4. For S255IR-SMA1 and S255N-SMA1 we give velocities and line widths of the most intense components.

The clumps are elongated; we indicate linear sizes as the geometric mean between the major and minor axes. The virial masses are obtained in the simplest way, assuming uniform spherical clouds as in Zinchenko et al. (1994). The same geometry is used to derive mean gas densities. It is worth noting that for all clumps the line widths greatly exceed expected thermal widths which hints at strong turbulence in these objects.

For the clumps investigated by Wang et al. (2011) our mass estimates are very close to their estimates. The virial masses

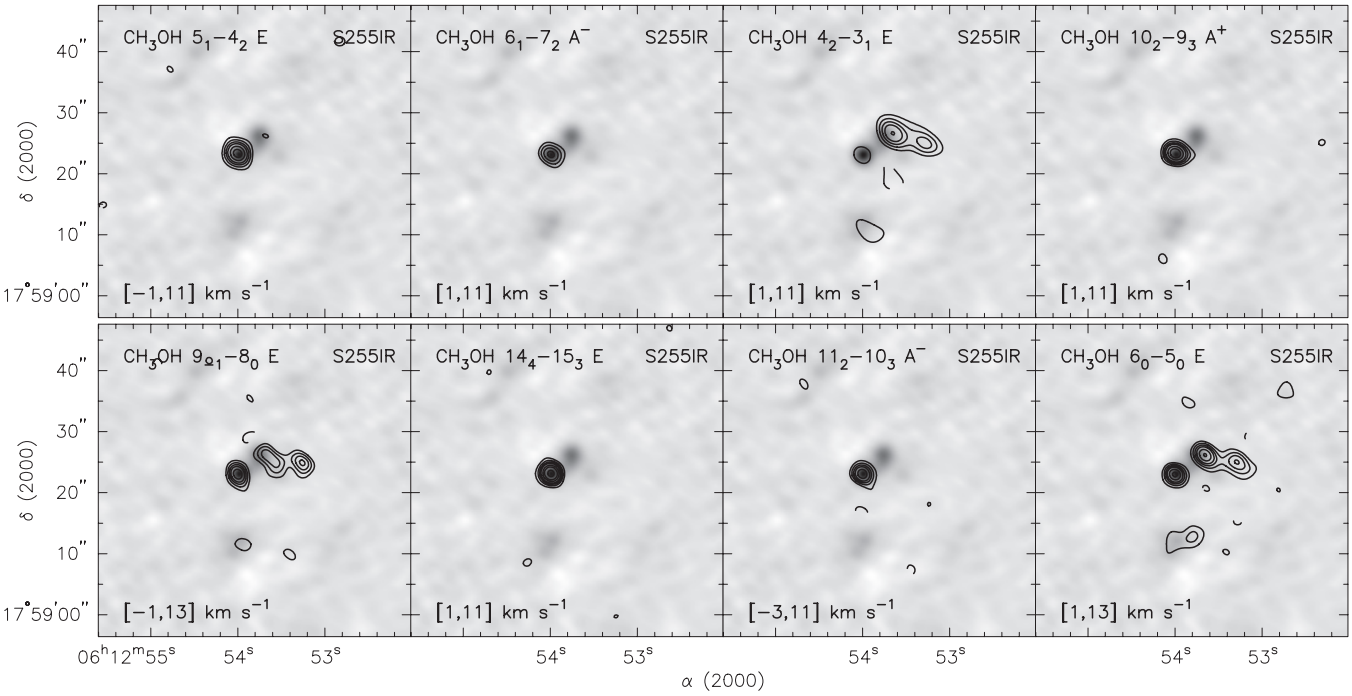

Figure 18. Maps of the CH_3OH integrated line emission in the S255IR area (contours) overlaid on the 1.1 mm continuum image. The velocity ranges are indicated at the bottom of the plots. The contour levels are $(-3, 3, 5, 7, 9, 12, 15, 20) \times 0.3$ Jy beam^{-1} km s^{-1} for the 5_1–4_2 E, 6_1–7_2 A$^-$, 10_2–9_3 A$^+$, and 14_4–15_3 E lines, and $(-3, 3, 5, 7, 9, 12, 15, 20) \times 0.6$ Jy beam^{-1} km s^{-1} for the other lines. The dashed contours show negative features due to the missing flux.

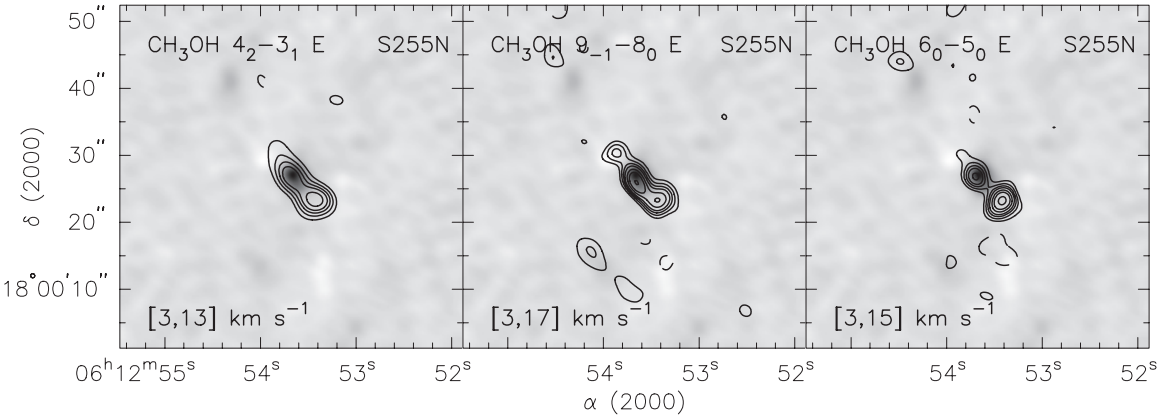

Figure 19. Maps of the CH_3OH integrated line emission in the S255N area (contours) overlaid on the 1.1 mm continuum image. The velocity ranges are indicated at the bottom of the plots. The contour levels are $(-3, 3, 5, 7, 9, 12, 15, 20) \times 0.6$ Jy beam^{-1} km s^{-1}. The dashed contours show negative features due to the missing flux.

for the major clumps in these areas (S255IR-SMA1, S255IR-SMA2, and S255N-SMA1) and for S255IR-SMA4 are close to the masses derived from the dust continuum emission (within a factor of ∼2). This means that these clumps are close to being in gravitational equilibrium. On the other hand, the virial masses of the weaker clumps in the S255N area in some cases are an order of magnitude greater than the masses obtained from the dust emission. In principle, these clumps could in truly be unbound and represent transient density enhancements produced by turbulence. However, estimates of their virial masses are rather uncertain, too. For example, the ammonia lines in S255IR-SMA5 are almost four times narrower than the $C^{18}O$ line which was used for the estimate of the virial mass. If we estimate the velocity dispersion from ammonia, the discrepancy between the virial mass and mass derived from the dust emission disappears for this clump. The difference in the line widths can be caused by the fact that the $C^{18}O$ emission is much more extended. Then, these clumps could be even colder than we assumed. We can conclude that the question of the stability of these clumps needs further investigation.

Our data show clusters of star-forming clumps in both S255IR and S255N. Using the data on clump velocities presented in Table 4 we can estimate virial masses of these clusters. These estimates give $M_{\rm vir} \sim 300\,M_\odot$ for S255IR and $M_{\rm vir} \sim 100\,M_\odot$ for S255N which is in reasonable agreement with their mass estimates based on single-dish observations of the dust emission (Zinchenko et al. 2009; Wang et al. 2011).

4.3. Molecular Clumps without Continuum Counterpart

In some cases, even quite strong molecular emission at velocities of the quiescent gas has no detectable continuum counterpart. For example, the ammonia emission in S255N is strong and extended toward the north in both the (1,1) and

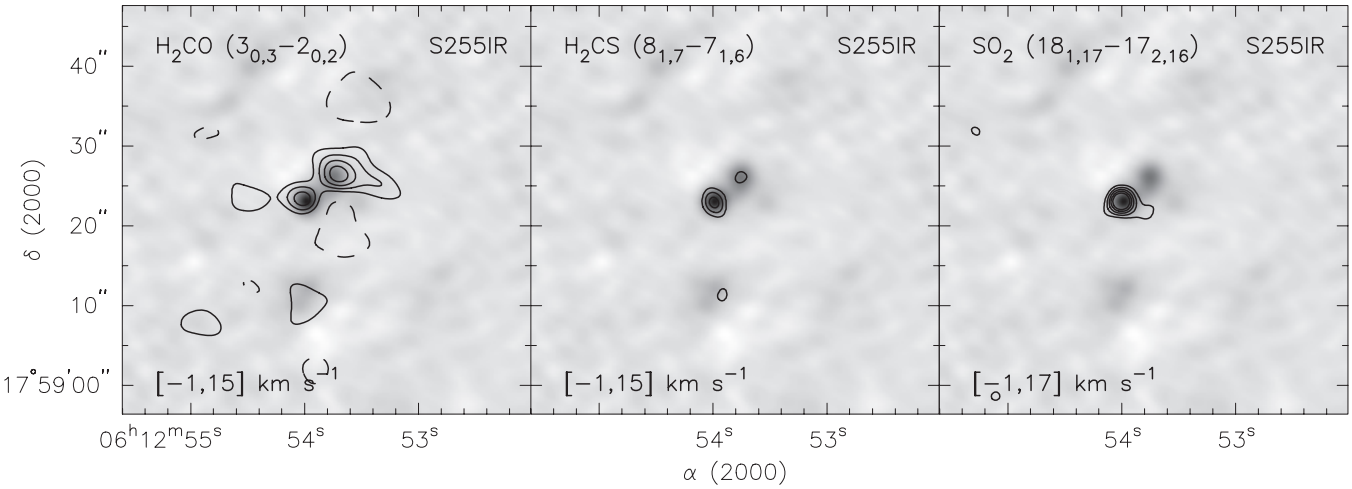

Figure 20. Maps of the H_2CO $3_{0,3}$–$2_{0,2}$, H_2CS $8_{1,7}$–$7_{1,6}$, and SO_2 $18_{1,17}$–$17_{2,16}$ integrated line emission in the S255IR area (contours) overlaid on the 1.1 mm continuum image. The velocity ranges are indicated at the bottom of the plots. The contour levels are $(-3, 3, 5, 7, 9) \times 0.6$ Jy beam^{-1} km s^{-1}. The dashed contours show negative features due to the missing flux.

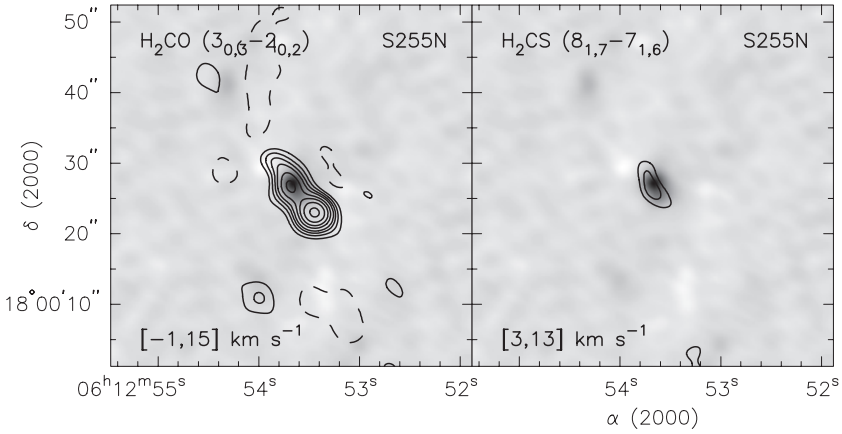

Figure 21. Maps of the H_2CO $3_{0,3}$–$2_{0,2}$ and H_2CS $8_{1,7}$–$7_{1,6}$ integrated line emission in the S255N area (contours) overlaid on the 1.1 mm continuum image. The velocity ranges are indicated at the bottom of the plots. The contour levels are $(-3, 3, 5, 7, 9, 12, 15, 19, 24) \times 0.6$ Jy beam^{-1} km s^{-1} for H_2CO $3_{0,3}$–$2_{0,2}$ and $(-3, 3, 5) \times 0.6$ Jy beam^{-1} km s^{-1} for H_2CS $8_{1,7}$–$7_{1,6}$. The dashed contours show negative features due to the missing flux.

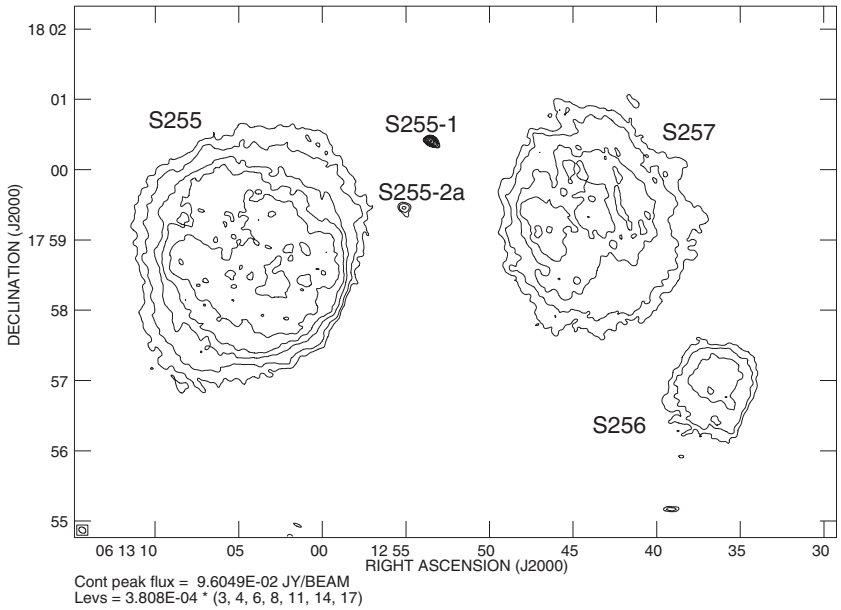

Figure 22. Our GMRT map of the investigated area at 610 MHz. It covers the extended H II regions S255, S256, and S257. Two compact sources in the center are associated with the S255IR and S255N star-forming cores.

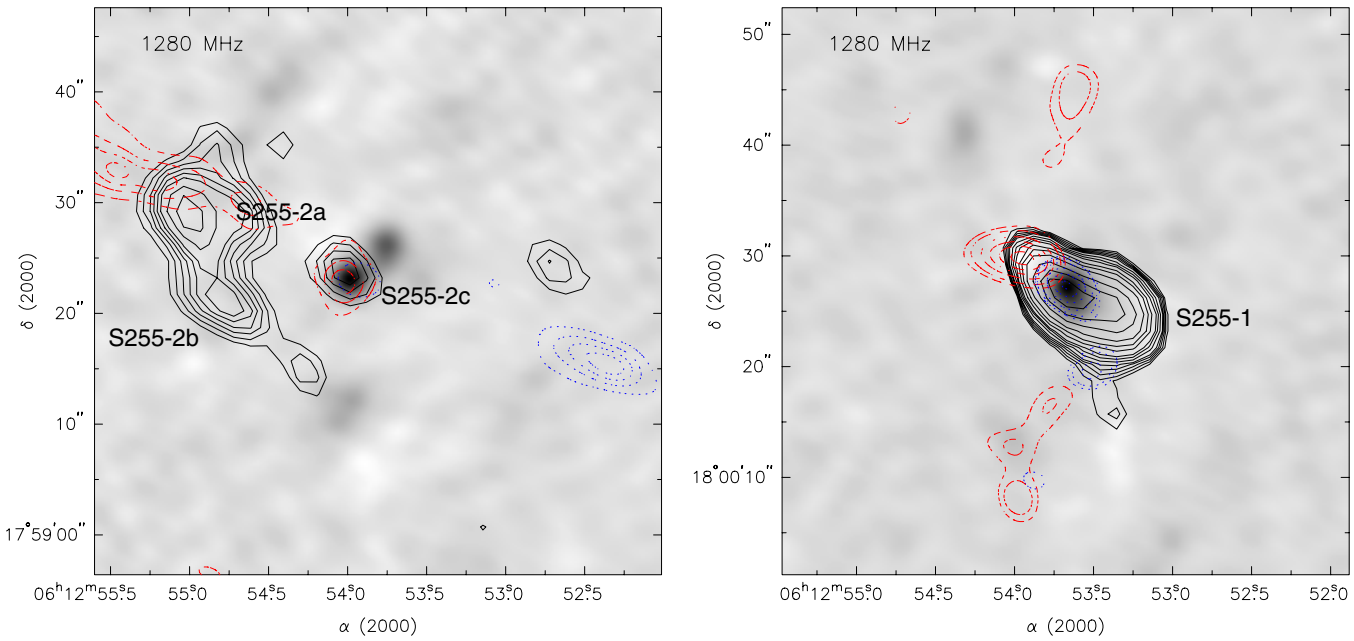

Figure 23. Maps of the 1280 MHz continuum emission in the S255IR (left panel) and S255N (right panel) areas (contours) overlaid on the 1.1 mm images. The contour levels are (3, 3.5, 4, 4.5, 5, 6, 7, 8, 10) × 0.22 mJy beam^{-1} for S255IR and (3, 3.5, 4, 4.5, 5, 6, 7, 8, 10, 12, 15, 20, 25, 30) × 0.22 mJy beam^{-1} for S255N. The dash-dotted (red in the online version) and dotted (blue in the online version) contours show the redshifted and blueshifted high-velocity CO emission, respectively. (A color version of this figure is available in the online journal.)

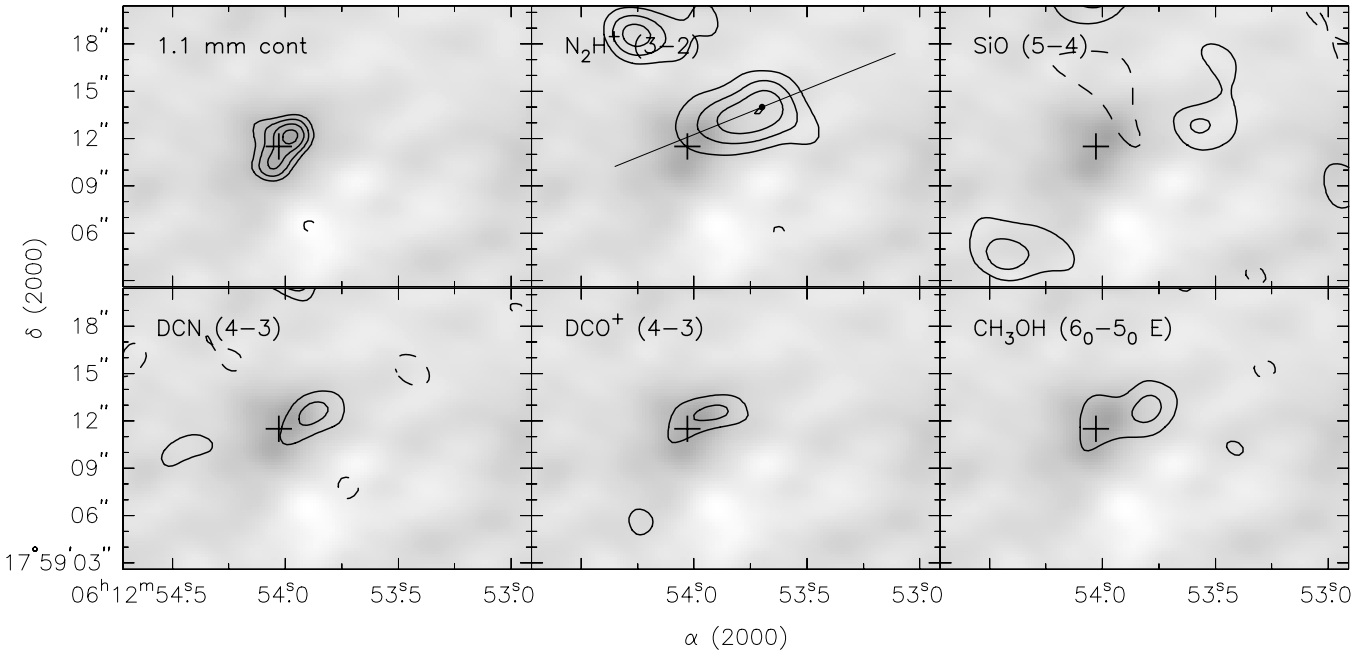

Figure 24. Maps of the 1.1 mm continuum emission and integrated line emission of several molecular species in the S255IR-SMA4 area (contours) overlaid on the 1.1 mm continuum image. The velocity ranges are the same as in Figures 2, 8, 10, and 18 for those species. The contour levels are the same as earlier for continuum, N_2H^+ and CH_3OH, and 1.5 times lower for SiO, DCN, and DCO^+ (in order to better show weaker features). The cross marks the position of S255IR-SMA4. The straight line in the N_2H^+ panel indicates the location of the position–velocity slice shown in Figure 25. The dot on this line corresponds to the zero offset in Figure 25.

(2,2) lines (see Figure 3). This emission occurs at distances up to ∼25″ (∼0.3 pc) from the continuum source. At the same time our own data and the results published by Wang et al. (2011) show that the ammonia emission is spatially close to the redshifted high-velocity CO emission lobe and is extended in the same direction. Moreover, a comparison of the NH_3 (1,1) and (2,2) maps shows that the intensity ratio $I(2,2)/I(1,1)$ increases toward this CO lobe, implying a temperature increase. These facts hint at a physical association between the ammonia emission and the high-velocity outflow, even though they do not coincide spatially or have the same velocity. A possible explanation is that in ammonia (and partly in N_2H^+ and DCO^+) we see the cold quiescent gas interacting with the high-velocity outflow. This interaction heats the gas, causing the observed temperature gradient. The absence of emission in other molecular lines probably means that these molecules are frozen onto dust grains. This assumption is consistent with the low kinetic temperature derived for this area. However, the picture

is further complicated by the fact that we see two kinematic components in ammonia (Figure 4) with significantly different temperatures (Section 3.2.1). An alternative explanation could be that one of the ammonia clumps is the driving source of the high-velocity outflow seen in CO. A point in favor of this interpretation is that the CO emission is not obviously associated with the SMA1 clump, while the ammonia emission is. The interpretation is hampered by the fact that we see no blueshifted high-velocity CO emission.

Another interesting zone of molecular emission without associated continuum emission is S255IR-N_2H^+(1). Wang et al. (2011) report methanol emission in the 8_{-1}–7_0 E transition and suggest that it is related to the shock heating excited by the outflow, and possibly is masing. However, our data show emission from many other lines, including N_2H^+, H_2CO, several methanol transitions, and probably NH_3 and DCO^+. This seems to rule out the hypothesis of specific excitation of the 8_{-1}–7_0 E methanol line and indicates the presence of an object with rather unusual properties. It is noteworthy that we detect no $C^{18}O$ or $C^{34}S$ emission in this area. At the same time, the temperature derived here from ammonia is rather high (∼50 K), which implies a presence of a heating source. This area apparently also needs further investigation.

Cyganowski et al. (2007) and Wang et al. (2011) mentioned one more area of strong molecular emission without a continuum counterpart shifted to southwest from S255N-SMA1 along the direction of the outflow. It is also seen in several of our maps (e.g., Figures 11 and 21).

4.4. Molecular Outflows

A description of high-velocity outflows in the S255IR and S255N areas based on CO $J = 2$–1 observations with the SMA was given by Wang et al. (2011). They identified one outflow in the S255IR area and at least one in S255N, mentioning a rather complicated structure for the high-velocity CO emission here, and not excluding the possibility of multiple outflows. Our data—in particular the SiO observations—shed new light on this question. First, the SiO data indicate that there are probably outflows originating from the weaker and presumably less-evolved clumps. As mentioned above, we almost certainly see outflows associated with the S255N-SMA3 and S255N-SMA5 clumps. An outflow related to the S255IR-SMA4 clump also seems probable. None of these objects show NIR, radio continuum, or maser emission, which implies a very early evolutionary stage.

Basic physical properties of outflows are usually derived from observations of CO and—preferably—^{13}CO and $C^{18}O$ (e.g. Cabrit & Bertout 1990, 1992; Henning et al. 2000; Zinchenko 2002). In our case we see the high-velocity CO $J = 2$–1 emission toward S255N-SMA3 and S255N-SMA5. However, neither ^{13}CO nor $C^{18}O$ are detected in the velocity ranges of the SiO outflows. We also do not see an emission in the lines of other potential outflow tracers (e.g. methanol) at these velocities. Therefore we use CO data to estimate physical parameters of these outflows assuming a small optical depth in the CO line wings. This assumption is most probably incorrect, which means that our estimates of the mass and mechanical parameters represent lower limits. Following the procedures outlined in the mentioned works we derive mass, momentum, energy, size, age, mass loss rate, and mechanical force for these outflows (Table 5). The inclination angle was assumed to be 45°. The outflows appear to be very young (a few hundred years). The mass loss rate and mechanical force are significantly lower than

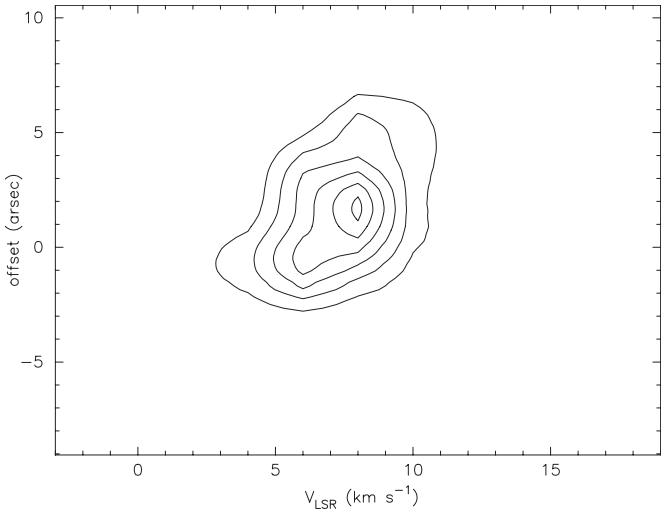

Figure 25. Position–velocity diagram for the N_2H^+ emission in the S255IR-SMA4 area along the line indicated in Figure 24.

in S255IR-SMA1 and S255N-SMA1, and comparable to those in S255S (Wang et al. 2011).

We cannot derive parameters for the possible outflow related to the S255IR-SMA4 clump since we cannot identify the relevant CO emission.

4.5. Chemical Features

One of the most remarkable features in our molecular maps is the absence of N_2H^+ emission from S255IR-SMA1. Any N_2H^+ emission from this clump is at least an order of magnitude weaker than that from SMA2. This fact cannot be explained by excitation effects and most probably implies a corresponding difference in the N_2H^+ column density and the N_2H^+ abundance, taking into account the similar total gas column densities for these clumps (Wang et al. 2011). A drop in N_2H^+ abundance in luminous massive cores was seen in our earlier single-dish observations (Pirogov et al. 2007; Zinchenko et al. 2009) and reported recently by others (e.g., Busquet et al. 2011; Reiter et al. 2011; Cortes 2011). The usual explanation for N_2H^+ depletion is its destruction by CO molecules released from dust grains at rising temperature. However, the $C^{18}O$ maps do not support this hypothesis. The $C^{18}O$ intensities are similar for SMA1 and SMA2, if not stronger toward the latter (Wang et al. 2011 and our data).

It is probably not coincidental that the DCO^+ distribution follows that of N_2H^+, as mentioned above. Both species apparently avoid ionized regions. This is also true for S255N and is consistent with our previous suggestion that the primary destruction mechanism for N_2H^+ in such objects is dissociative recombination due to an enhanced ionization fraction (Pirogov et al. 2007; Zinchenko et al. 2009). At the same time in S255N there is a noticeable difference between the DCO^+ and N_2H^+ maps: There is no DCO^+ emission toward the brightest N_2H^+ peak. In principle this might be caused by temperature distribution in this area—an enhanced temperature would reduce the abundance of deuterated molecules. It is worth noting that the NH_3 (2,2) emission has a peak here while emission peaks of other deuterated species (DCN and DNC) are also shifted from the N_2H^+ peak.

Another interesting feature is the rather strong DCN emission from several clumps, including S255IR-SMA1, which is apparently hot, as mentioned above. Although there are

Table 5
Parameters of the Outflows in S255N-SMA3 and S255N-SMA5 (Mass, Momentum, Energy, Size, Age, Mass Loss Rate, and Mechanical Force)

Name	M ($M_\odot$)	P ($M_\odot$ km s^{-1})	E (erg)	Size (pc)	t (yr)	$\dot{M}$ ($M_\odot$ yr^{-1})	F ($M_\odot$ km s^{-1} yr^{-1})
S255N-SMA3	0.003	0.15	8×10^{43}	0.009	200	2×10^{-5}	8×10^{-4}
S255N-SMA5	0.012	0.36	10^{44}	0.012	400	3×10^{-5}	9×10^{-4}

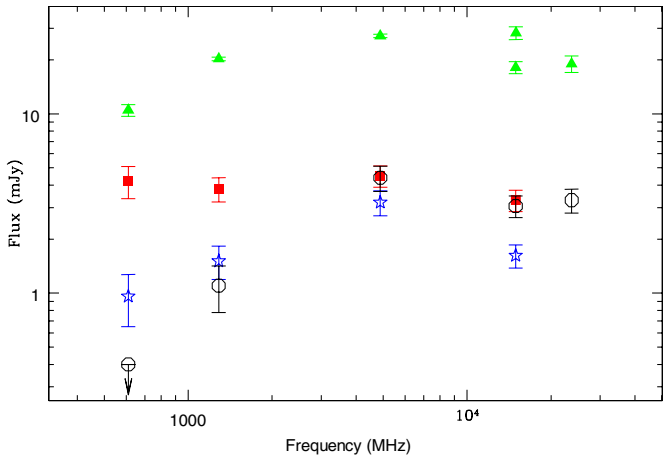

Figure 26. Spectra of S255-1 (triangles), S255-2a (squares), S255-2b (stars), and S255-2c (circles). The data at 610 MHz, 1280 MHz, and 23.7 GHz are from the present work, at 5 GHz from Snell & Bally (1986), at 15 GHz from Snell & Bally (1986) (S255-1) and Ojha et al. (2011).

(A color version of this figure is available in the online journal.)

observations of rather high DCN abundances in warm (50–75 K), dense ($n \sim 10^7$ cm^{-3}) clumps (Leurini et al. 2006; Parise et al. 2009) which were successfully explained by chemical models (Roueff et al. 2007; Parise et al. 2009), it is hard to expect the same at the temperature of ∼150 K derived for S255IR-SMA1. Recent modeling by Albertsson et al. (2011) shows that the DCN/HCN abundance ratio sharply drops at temperatures $\gtrsim$80 K. Possible explanations for a high DCN abundance in this clump might presume a significant amount of relatively cold gas in this clump or a very young age, with insufficient time to change the isotopic ratio. The required time can be less than 10^4 years as discussed by Hatchell et al. (1998). Inspection of Figures 8 and 10 shows that the peak of the DCN emission is noticeably shifted from the continuum peak and SiO emission peak. Most probably DCN traces cold material adjacent to the hot core. The density of this material should be high in order to explain the observed intensity ratio of the DCN $J = 3$–2 and $J = 4$–3 transitions. Our temperature estimates from the ammonia observations show a presence of a relatively cold component in S255IR-SMA1.

In S255N the DCN emission is noticeably stronger than in S255IR; we also detected DNC here. In the framework of time-dependent chemistry (e.g., Hatchell et al. 1998) this may indicate that S255N is younger than S255IR. This is also consistent with a lower temperature of S255N in respect to S255IR as found from ammonia observations. However, we need estimates of the DCN/HCN abundance ratios.

As mentioned above we did not detect N_2D^+ in either S255IR or S255N. An upper limit (3σ) on the N_2D^+ brightness implies a limit on the intensity ratio $I(N_2D^+)/I(N_2H^+) \lesssim 0.1$ for the brightest N_2H^+ emission peaks. In cold dark clouds this ratio can reach the values of ∼0.25 but drops to $\lesssim$0.1 at temperatures $\gtrsim$25 K (e.g. Emprechtinger et al. 2009). In our case, when temperature estimates for the bright N_2H^+ emission peaks are available, they show higher values. Therefore, the non-detection of N_2D^+ is consistent with our temperature estimates.

Some other chemical peculiarities related to molecular emission not associated with a noticeable dust continuum have been mentioned above (in particular the ammonia source S255N-NH_3 in the northern part of the S255N area, some of the N_2H^+ sources, etc.).

4.6. Properties of the Radio Continuum Sources

Our GMRT (Figures 23) and available VLA archival data show the presence of several centimeter and decimeter wave continuum sources. The sources S255-2a and S255-2b identified earlier by Snell & Bally (1986) are associated with NIR objects (Ojha et al. 2011) that are classified as B-type stars and apparently represent compact H II regions excited by these stars. It is interesting that we do not see any molecular or dust emission associated with these sources. The high-velocity CO redshifted lobe is close to S255-2a but it is unclear whether there is a physical association. Possibly the parental cloud material of these stars has already been dispersed, indicating a relatively large age.

The source S255-2c is associated with S255IR-SMA1. It has extensions in the directions of both redshifted and blueshifted lobes of the molecular outflow, more pronounced at low frequencies. This indicates a gradient in the emission measure. Apparently at least part of the emission is associated with ionized gas in the outflow. Ojha et al. (2011) concluded that this source is younger than S255-2a and 2b. This is consistent with our data, which indicate the presence of a hot molecular core.

In S255N the low frequency radio continuum maps also show an extension in the direction of the outflow lobe, as in S255IR. Presumably this also is an indication of emission from ionized, outflowing gas.

The spectra of all the sources in the range from 610 MHz to 23.7 GHz are plotted in Figure 26 using the flux densities from the present observations, data from Snell & Bally (1986) and Ojha et al. (2011). The flux density at 15 GHz is different from that presented by Ojha et al. (2011) since the primary beam correction was not applied in that paper. The noise of the map at 610 MHz is used as the upper limit for the source S255-2c and the errors at 15 GHz are considered to be 15% (D. K. Ojha et al. 2011, private communication). It should be noted that these measurements are obtained from radio continuum maps made with different approaches and with different angular resolutions. For example, Ojha et al. (2011) estimated positions and flux densities by fitting elliptical Gaussian model components, assuming the sources to be point-like, whereas the total flux density reported by Snell & Bally (1986) was obtained by integrating over the region within the 3σ limit.

The structure of S255N is quite complex. The high resolution (∼1 arcsec) 3.6 cm VLA map by Cyganowski et al. (2007) resolved the UC H II region into three components, with an arc, a point source, and an extended tail, which add uncertainty in the

estimation of fluxes. However, the general shape of the spectral energy distribution in Figure 26 is consistent with free–free emission from thermal plasma.

The spectra show that the emission of S255-2a is optically thin throughout this frequency range, while the other sources become optically thick at the lowest frequencies. An expected flux for S255-2a at 23.7 GHz is about the same as for S255-2c. However S255-2a is more extended (Table 3) and therefore its brightness should be lower than that of S255-2c. This can be the reason for its non-detection at this frequency. S255-2b is noticeably weaker and apparently below our detection limit at 23.7 GHz.

Using the formulae for free–free emission from Lang (1999) and assuming an electron temperature of 10^4 K we can estimate the emission measure for these objects. For S255-2a with a turnover frequency of $\nu_T \lesssim 600$ MHz, we obtain EM $\lesssim 10^6$ pc cm^{-6}. Ojha et al. (2011) from their measured fluxes and sizes derived EM $\sim 1.5 \times 10^6$ pc cm^{-6} for this source, in agreement with our estimate. For S255-2b, S255-2c, and S255-1 the turnover frequency seems to be in the range of 2–3 GHz, which implies EM $\sim$ (1–2.5) $\times 10^7$ pc cm^{-6}. For S255-2c and S255-1 these estimates are reasonably close to those derived by Ojha et al. (2011). However, in the case of S255-2b, Ojha et al. (2011) obtained a significantly lower estimate for the emission measure which corresponds to the turnover frequency of about 1 GHz. The reasons for this discrepancy are not clear. Perhaps the flux of S255-2b at 5 GHz is overestimated.

5. CONCLUSIONS

1. We detected several new clumps in the S255IR and S255N areas by their millimeter wave continuum emission. They are also detected in several molecular lines. Temperatures of these clumps found from ammonia observations are ∼20 K and their masses are estimated at a few solar masses. These clumps have almost no association with NIR or radio continuum sources, which implies a very early stage of evolution. At the same time, our SiO and other molecular data indicate the presence of high-velocity outflows related to some of these clumps. The outflows associated with S255N-SMA3 and S255N-SMA5 are apparently very young—a few hundred years only. The line widths of the clumps greatly exceed the expected thermal widths, suggesting significant turbulence in these objects.
2. In some cases there is strong molecular emission at the velocity of the quiescent gas, yet with no detected continuum counterpart. The nature of these sources is not clear. Some of them (e.g., the ammonia source in the northern part of S255N) may represent very cold gas not detectable in the dust continuum. Emission from CO and other molecules would be absent in this case, because they would be frozen onto dust grains. This assumption is consistent with the low kinetic temperature derived for this area from the ammonia observations.
3. N_2H^+ and DCO^+ apparently avoid ionized regions. There is no detectable N_2H^+ emission associated with the SMA1 clump in S255IR (which contains a hot core and also ionized gas) implying a significant drop in the N_2H^+ abundance. There is no sign that this is caused by CO evaporation.
4. We detected rather strong emission in lines of deuterated species—DCN and DCO^+—in both S255IR and S255N (in S255N the DCN $J = 3$–2 line was seen earlier by Cyganowski et al. 2007). In S255N a DNC emission line is also detected. In S255IR the DCN emission is also quite strong in the vicinity of the hot core. This implies either the presence of a significant amount of cold gas or a very young age for this hot core, insufficient to have changed the isotopic ratio.
   The DCO^+ distribution is significantly different from that of DCN and qualitatively resembles that of N_2H^+. In particular, both species avoid ionized regions and both are observed toward the S255N-SMA6 clump (in contrast to most other molecules).
5. There is no molecular material associated with the S255-2a and S255-2b radio continuum sources, which are compact H II regions excited by B type stars. Possibly the parental material of these stars has already been dispersed, indicating a relatively large age for these objects.

We are very grateful to the anonymous referee for the helpful comments and suggestions, and to Andrej Sobolev and Svetlana Salii for discussions of the methanol data. This work was supported by the Russian Academy of Sciences (Research program No. 17 of the Department of Physical Sciences), Russian Foundation for Basic Research (grants RFBR 08-02-92001-NSC, RFBR 11-02-92690-Ind, RFBR 12-02-00861), National Science Council of Taiwan (grant NSC 97-2923-M-001-004-MY3), DGAPA, UNAM project IN101310, and Department of Science and Technology of the Government of India (grant DST-RFBR RUSP-1107). The research has made use of the SIMBAD database, operated by CDS, Strasbourg, France.

REFERENCES

Albertsson, T., Semenov, D. A., & Henning, T. 2011, arXiv:1110.2644
Busquet, G., Estalella, R., Zhang, Q., et al. 2011, A&A, 525, A141
Cabrit, S., & Bertout, C. 1990, ApJ, 348, 530
Cabrit, S., & Bertout, C. 1992, A&A, 261, 274
Cortes, P. C. 2011, ApJ, 743, 194
Cragg, D. M., Sobolev, A. M., & Godfrey, P. D. 2005, MNRAS, 360, 533
Crowther, P. A., & Conti, P. S. 2003, MNRAS, 343, 143
Cyganowski, C. J., Brogan, C. L., & Hunter, T. R. 2007, AJ, 134, 346
Emprechtinger, M., Caselli, P., Volgenau, N. H., Stutzki, J., & Wiedner, M. C. 2009, A&A, 493, 89
Harju, J., Walmsley, C. M., & Wouterloot, J. G. A. 1993, A&AS, 98, 51
Hatchell, J., Millar, T. J., & Rodgers, S. D. 1998, A&A, 332, 695
Henning, T., Lapinov, A., Schreyer, K., Stecklum, B., & Zinchenko, I. 2000, A&A, 364, 613
Ho, P. T. P., & Townes, C. H. 1983, ARA&A, 21, 239
Howard, E. M., Pipher, J. L., & Forrest, W. J. 1997, ApJ, 481, 327
Itoh, Y., Tamura, M., Suto, H., et al. 2001, PASJ, 53, 495
Kurtz, S., Churchwell, E., & Wood, D. O. S. 1994, ApJS, 91, 659
Lang, K. R. (ed.) 1999, Astrophysical Formulae (New York: Springer)
Leurini, S., Rolffs, R., Thorwirth, S., et al. 2006, A&A, 454, L47
Lintott, C. J., Viti, S., Rawlings, J. M. C., et al. 2005, ApJ, 620, 795
Mangum, J. G., Wootten, A., & Mundy, L. G. 1992, ApJ, 388, 467
Miralles, M. P., Salas, L., Cruz-Gonzalez, I., & Kurtz, S. 1997, ApJ, 488, 749
Ojha, D. K., Samal, M. R., Pandey, A. K., et al. 2011, ApJ, 738, 156
Ossenkopf, V., & Henning, T. 1994, A&A, 291, 943
Parise, B., Leurini, S., Schilke, P., et al. 2009, A&A, 508, 737
Pirogov, L., Zinchenko, I., Caselli, P., & Johansson, L. E. B. 2007, A&A, 461, 523
Reiter, M., Shirley, Y. L., Wu, J., et al. 2011, ApJS, 195, 1
Roueff, E., Parise, B., & Herbst, E. 2007, A&A, 464, 245
Russeil, D., Adami, C., & Georgelin, Y. M. 2007, A&A, 470, 161
Rygl, K. L. J., Brunthaler, A., Reid, M. J., et al. 2010, A&A, 511, A2
Salii, S. V., & Sobolev, A. M. 2006, Astron. Rep., 50, 965
Sault, R. J., Teuben, P. J., & Wright, M. C. H. 1995, in ASP Conf. Ser. 77, Astronomical Data Analysis Software and Systems IV, ed. R. A. Shaw, H. E. Payne, & J. J. E. Hayes (San Francisco, CA: ASP), 433
Scoville, N. Z., Carlstrom, J. E., Chandler, C. J., et al. 1993, PASP, 105, 1482
Snell, R. L., & Bally, J. 1986, ApJ, 303, 683

Sobolev, A. M. 1993, in Astrophysical Masers, ed. A. W. Clegg & G. E. Nedoluha (Lecture Notes in Physics, Vol. 412; Berlin: Springer), 215
Sutton, E. C., Sobolev, A. M., Salii, S. V., et al. 2004, ApJ, 609, 231
Swarup, G., Ananthakrishnan, S., Kapahi, V. K., et al. 1991, Curr. Sci., 60, 95
Voronkov, M. A., Caswell, J. L., Ellingsen, S. P., et al. 2012, arXiv:1203.5492
Walmsley, C. M., & Ungerechts, H. 1983, A&A, 122, 164
Wang, Y., Beuther, H., Bik, A., et al. 2011, A&A, 527, A32
Zinchenko, I., Caselli, P., & Pirogov, L. 2009, MNRAS, 395, 2234
Zinchenko, I., Forsstroem, V., Lapinov, A., & Mattila, K. 1994, A&A, 288, 601
Zinchenko, I., Henning, T., & Schreyer, K. 1997, A&AS, 124, 385
Zinchenko, I. I. 2002, Astron. Lett., 28, 316